aerospace

MDPI

Article

Rapid Approximation of Low-Thrust Spacecraft Reachable Sets within Complex Two-Body and Cislunar Dynamics

Sean Bowerfind and Ehsan Taheri *

Department of Aerospace Engineering, Auburn University, Auburn, AL 36832, USA
* Correspondence: ezt0028@auburn.edu

Abstract: The reachable set of controlled dynamical systems is the set of all reachable states from an initial condition over a certain time horizon, subject to operational constraints and exogenous disturbances. In astrodynamics, rapid approximation of reachable sets is invaluable for trajectory planning, collision avoidance, and ensuring safe and optimal performance in complex dynamics. Leveraging the connection between minimum-time trajectories and the boundary of reachable sets, we propose a sampling-based method for rapid and efficient approximation of reachable sets for finite- and low-thrust spacecraft. The proposed method combines a minimum-time multi-stage indirect formulation with the celebrated primer vector theory. Reachable sets are generated under two-body and circular restricted three-body (CR3B) dynamics. For the two-body dynamics, reachable sets are generated for (1) the heliocentric phase of a benchmark Earth-to-Mars problem, (2) two scenarios with uncertainties in the initial position and velocity of the spacecraft at the time of departure from Earth, and (3) a scenario with a bounded single impulse at the time of departure from Earth. For the CR3B dynamics, several cislunar applications are considered, including L1 Halo orbit, L2 Halo orbit, and Lunar Gateway 9:2 NRHO. The results indicate that low-thrust spacecraft reachable sets coincide with invariant manifolds existing in multi-body dynamical environments. The proposed method serves as a valuable tool for qualitatively analyzing the evolution of reachable sets under complex dynamics, which would otherwise be either incoherent with existing grid-based reachability approaches or computationally intractable with a complete Hamilton–Jacobi–Bellman method.

Keywords: reachability; low thrust; indirect; optimization; trajectory; cislunar; halo orbit; two-body; Lunar; NRHO

Citation: Bowerfind, S.; Taheri, E. Rapid Approximation of Low-Thrust Spacecraft Reachable Sets within Complex Two-Body and Cislunar Dynamics. *Aerospace* **2024**, *11*, 380. https://doi.org/10.3390/aerospace11050380

Academic Editor: Andrzej Łukaszewicz

Received: 4 April 2024
Revised: 5 May 2024
Accepted: 6 May 2024
Published: 9 May 2024

1. Introduction

Optimal control techniques are used extensively for solving challenging practical engineering problems [1–3] and for trajectory optimization tasks [4,5]. Optimal control and robotics applications frequently use reachable set theory as a metric to assess cost and safety. In astrodynamics, solutions to reachability problems are useful for determining the spacecraft states that will lead to an inevitable collision or encounter, regardless of future collision avoidance maneuvers [6]. Knowledge of an object's reachable set can be used to perform evasive maneuvers (in the case of the International Space Station) or orbital rendezvous and docking [7]. Beyond low-Earth orbits, the ability to compute reachable sets is advantageous for cislunar [8] and interplanetary mission design, as reachable sets provide mission designers with information regarding future planetary encounters from a given set of initial conditions [9]. Future NASA deep-space missions with numerous planetary flybys could substantially benefit from knowledge about the reachable set of their respective spacecraft [10].

A reachable set is defined as the set of all states that can be reached from a given initial condition within a specified time horizon. Determining the reachable set, however, is a problem that suffers from the "curse of dimensionality" since the Hamilton–Jacobi–Bellman (HJB) equation [11], a partial differential equation (PDE), has to be solved to determine

the reachable sets. The exact reachable set can be found by computing the zero-level set of the viscosity solution of an HJB problem [12]. Across all classes of systems, linear, time-invariant systems have been the most thoroughly analyzed. Results of studies of linear, time-invariant systems have shown that an analytical solution to the reachable set exists for cases of convex polyhedral state and control spaces [13]. However, once constraints that lead to a nonconvex control space are introduced (common in astrodynamics problems), analytical solutions do not exist, and numerical methods (i.e., direct and indirect) must be used instead [2]. Indirect methods solve the viscosity solution of the HJB, while direct methods discretize the continuous-time optimal control problems (OCPs) into parametric nonlinear optimization problems [14,15]. In 1980, Vinter showed how to approximate the reachability problem as a convex optimization problem and conducted the first study to demonstrate how to approximate the reachable set using a series of smoothing functions [16]. Determination of the reachable set becomes an increasingly difficult problem as the dimensionality of the problem and the number of control signals increases [17]. It becomes computationally infeasible to compute every possible trajectory variation through simulation alone [18]. Modern research has expanded these approximation techniques to generate over- or under-approximations for continuous-time linear systems [19], general nonlinear dynamics [20], and more complex systems [21].

In astrodynamics, reachability problems for both chemical rockets and electric propulsion spacecraft are studied. Chemical rocket propulsion reachability largely focuses on single-impulse maneuvers and has been studied within the cislunar environment [22–35]. Electric propulsion or continuous-thrust reachability problems have been proposed for low-Earth, cislunar, and interplanetary mission planning applications [15,17,36–39]. Other methods attempt to calculate reachable sets by utilizing passive ΔV maneuvers such as gravity assists and solar radiation pressure in small-body proximity operations [7,9,10,40,41].

For chemical propulsion systems, an on-orbit range equation was derived for ΔV with J2 perturbations [42]. These results were used in [34] to develop closed-form impulsive control schemes by computing a minimum ΔV and then solving a geometric path-planning problem. The reachable domain for spacecraft with ellipsoidal ΔV distributions was also studied in [43]. For electric propulsion systems, Ref. [44] derived continuous indirect equations incorporating ellipsoidal uncertainty. Several works have formulated OCPs and directly solved the HJB equation to generate reachable sets in the CR3BP over short time horizons [45,46]. Specifically, Ref. [46] took a Poincaré section approach and detailed analysis with invariant manifolds, and [45] utilized a power-series approximation of the HJB to determine periodic orbit transfer trajectories. More recently, a cross-disciplined reachability-based trajectory design (RTD), developed by Kousik, has been used to perform safe path planning for quadcopters, wheeled vehicles, and robotic manipulators [47,48]. RTD computes the forward reachable set of a vehicle offline using zonotope reachability [49]. The forward reachable set is used in real time to perform obstacle avoidance maneuvering by comparing the forward reachable set with an environment map that dictates the safe set. RTD uses this method to perform path planning in real time before feeding the safe trajectory to a low-level tracking controller.

The boundary of reachable sets of low-thrust trajectories can be characterized with minimum-time trajectories [50]. For a spacecraft equipped with a low-thrust propulsion system, minimum-time maneuvers require the propulsion system to operate at its maximum thrust level, and only the direction of the thrust vector is subject to variations across the reachable set. In fact, there is a duality between minimum-time and minimum-thrust solutions [50], which allows one to view the reachability of a state or set of states by modifying the propulsion system parameters. For a fixed time horizon and specified thrust parameters, the set of states interior to the boundary of reachable sets will require a bang-bang control profile and correspond to minimum-fuel trajectories [43].

The main contributions of the paper are as follows. First, we propose a rapid reachable set approximation algorithm using an indirect multi-stage formulation (IMF) for solving OCPs. Note that we only consider the boundary of reachable sets. The proposed algorithm

leverages the theoretical connection between minimum-time trajectories and the boundary of the reachable sets. This connection leads to noticeable algorithmic simplification and speedup compared to the minimum-fuel method proposed in [51–53]. This algorithm requires no initial guess, and only one first-order forward-in-time propagation of the nonlinear equations of motion is required for each sample. Second, we present the low-thrust reachability results for interplanetary trajectory optimization. In particular, minimum-time, rendezvous-type, and Earth-to-Mars maneuvers for a low-thrust spacecraft are presented. We show how the results can be used to rapidly determine position and velocity reachability subject to additional initial boundary constraints for a low-thrust Earth-to-Mars rendezvous trajectory optimization problem. Third, we apply the low-thrust reachability to a number of orbits in the CR3B problem (CR3BP) of the Earth–Moon system. We demonstrate the versatility of this approach by generating novel results on the reachable set for a low-thrust spacecraft in cislunar space. We illustrate the unique evolution of the reachable set for an L2 Halo orbit and the Lunar Gateway 9:2 NRHO. The final contribution of this paper is to offer theoretical insights into the behavior and evolution of the reachable sets in the CR3BP. We show empirically that the reachable sets are connected to invariant manifolds of periodic orbits.

The remainder of this paper is organized as follows. First, the IMF OCP is introduced in Section 2.1, which precedes discussions on the two-body equations of motion in Section 2.2, the CR3BP in Section 2.3, a derivation of minimum-time optimal control relations in Section 2.4, and details on the application of initial boundary conditions in Section 2.5. Next, we outline the rapid reachable set determination algorithm in Section 3. Finally, the results are presented for the two-body dynamics in Section 4 and for the CR3BP in Section 5. We add remarks on invariant manifolds in Section 5.4 to explain some low-thrust reachable set trends identified within the CR3BP. Section 6 presents the conclusions of this paper. Please note that in the remainder of this paper, vectors are denoted by boldface letters.

2. Indirect Multi-Stage Formulation of Optimal Control Problems

2.1. Indirect Multi-Stage Formulation

An IMF of OCPs is adopted, which offers notable computational advantages since IMF allows for dynamics, constraints, and even cost functions to change between different stages. This is an important feature for the introduction of initial boundary conditions since the incorporation of boundary conditions is achieved through a different cost function to account for any mass discrepancies due to an impulse maneuver (see Section 2.5). The other reason for using an IMF is the ability to derive analytical expressions for control, which simplifies the solution procedure.

At its core, the IMF divides a complete trajectory into a series of stages but "connects" each stage through a sequence of equality constraints (see Figure 1). Each stage receives inputs of the states and controls from the previous stage but independently optimizes control over only its respective stage [54]. Please note that the IMF is used for deriving the required rigorous optimality relations associated with minimum-time trajectory optimization problems. These relations are later used within a backward-forward framework to determine reachable sets. The entire trajectory can be discretized into N stages, and the i-th stage (for $i \in \{1, \cdots, N\}$) can be modeled with its dynamical system consisting of states, $\boldsymbol{x} \in \mathbb{R}^{n_x}$; controls, $\boldsymbol{u} \in \mathbb{R}^{n_u}$; and parameters, $\boldsymbol{p} \in \mathbb{R}^{n_p}$, where the superscript denotes the stage index as,

$$\boldsymbol{x}^{i+1} = \boldsymbol{F}^i\left(\boldsymbol{x}^i, t^i, \boldsymbol{u}^i; \boldsymbol{p}\right), \quad \text{with} \quad \boldsymbol{F}^i = \boldsymbol{x}^i + \int_{t_i}^{t_{i+1}} \dot{\boldsymbol{x}} dt = \boldsymbol{x}^i + \int_{t_i}^{t_{i+1}} \boldsymbol{f}^{i-1}(\boldsymbol{x}, t, \boldsymbol{u}; \boldsymbol{p}) dt. \quad (1)$$

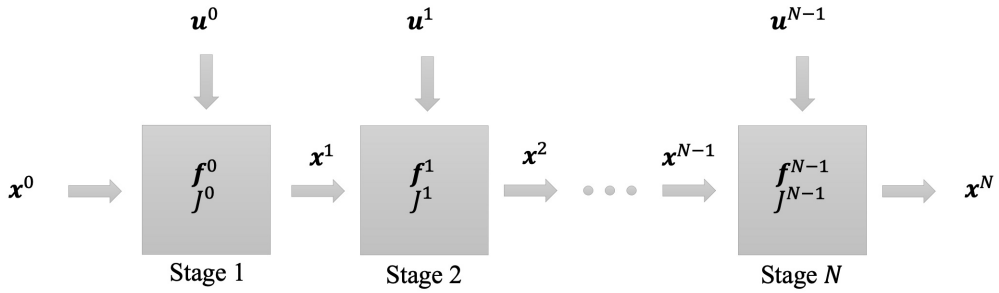

Figure 1. Flowchart for a multi-stage formulation.

The IMF solves OCPs recursively; that is, stage $i = 1$ is solved first, then $i = 2, \cdots, i = N$ until the solutions to all stages are computed. The derivation of the optimal control expressions is similar to continuous-time indirect formulations, except for some additional notation bookkeeping to track stages. The cost function for an IMF can be written as

$$J = \phi\left(\boldsymbol{x}^N, N\right) + \sum_i L^i\left(t^i, \boldsymbol{x}^i, \boldsymbol{u}^i\right), \tag{2}$$

where ϕ denotes the final cost and $L(\cdot)$ is the stage cost evaluated over the time horizon of each independent stage. The Hamiltonian of the complete trajectory can be written as the summation over the Hamiltonian of individual stages,

$$H = \sum_i H^i, \quad \text{with} \quad H^i = \left(\boldsymbol{\lambda}^{i+1}\right)^\top \boldsymbol{F}^i + L^i + \sum_k v_k C_k. \tag{3}$$

The costate vector, $\boldsymbol{\lambda} \in \mathbb{R}^{n_x}$, is specified with an $i+1$ superscript for convenience in the implementation of the algorithm, which includes a backward-in-time integration for the costates. In Equation (3), C_k and v_k indicate the k-th path constraint and its associated Lagrange multiplier (dimension of constraints, k, depends on the problem and the constraints). For each stage, partial derivatives of the Hamiltonian with respect to states and controls can be formed (note that in discrete form, we have $\boldsymbol{\lambda}^i = \partial H^i / \partial \boldsymbol{x}$; see Chapter 2 in [54]) as

$$\begin{aligned} \boldsymbol{\lambda}^i = \frac{\partial H^i}{\partial \boldsymbol{x}} &= \left(\boldsymbol{F}_{\boldsymbol{x}}{}^i\right)^\top \boldsymbol{\lambda}^{i+1} + L^i_{\boldsymbol{x}} + \sum_k v_k C_{k,\boldsymbol{x}}, \\ \frac{\partial H^i}{\partial \boldsymbol{u}} &= H^i_{\boldsymbol{u}} = \mathbf{0} = \left(\boldsymbol{F}_{\boldsymbol{u}}{}^i\right)^\top \boldsymbol{\lambda}^{i+1} + L^i_{\boldsymbol{u}} + \sum_k v_k C_{k,\boldsymbol{u}}. \end{aligned} \tag{4}$$

2.2. Two-Body Equations of Motion

For the first results presented in this paper, the heliocentric phase of an Earth-to-Mars rendezvous problem (with zero hyperbolic excess velocity) is considered, and third-body perturbations are ignored. Let $\boldsymbol{r} \in \mathbb{R}^3$ and $\boldsymbol{v} \in \mathbb{R}^3$ denote the position and velocity vectors, respectively. Let $\boldsymbol{x} = [\boldsymbol{r}^\top, \boldsymbol{v}^\top]^\top$ denote the state vector, and let $\hat{\boldsymbol{\alpha}}$ denote the thrust-steering unit vector. The state dynamics can be written as [55]

$$\dot{\boldsymbol{x}} = \begin{bmatrix} \dot{\boldsymbol{r}} \\ \dot{\boldsymbol{v}} \end{bmatrix} = \begin{bmatrix} \boldsymbol{v} \\ -\frac{\mu}{||\boldsymbol{r}||^3}\boldsymbol{r} + \frac{T_{\max}}{m}\hat{\boldsymbol{\alpha}}\delta \end{bmatrix}, \tag{5}$$

where μ denotes the gravitational parameter of the Sun; $c = I_{\text{sp}} g_0$ is the net exhaust velocity, with I_{sp} denoting the specific impulse; and g_0 is the gravitational acceleration at the Earth's surface. In Equation (5), $T_{\max}$ is the maximum thrust of the propulsion system operating in a thrust direction, $\hat{\boldsymbol{\alpha}} \in \mathbb{R}^3$, with a throttle setting of $\delta \in [0, 1]$. In a minimum-fuel solution [56], the optimal control of a low-thrust propulsion system will involve finding

both $\hat{\boldsymbol{\alpha}}$ and δ; however, for a minimum-time solution, it is known that the engine has to operate at maximum throttle during the entire trajectory ($\delta(t) = 1 \; \forall t \in [t_0, t_f]$) [57]. Thus, different minimum-time trajectories can be generated by varying thrust directions, $\hat{\boldsymbol{\alpha}}$, all of which characterize the low-thrust reachable set. The spacecraft mass, m, can be calculated as $m(t) = m_0 - \frac{T_{\max}}{c}(t - t_0)$. This minimum-time formulation leads to the extremal control vector, $\boldsymbol{u} \in \mathbb{R}^3$, which can be simply stated as

$$\boldsymbol{u}(t) = \hat{\boldsymbol{\alpha}}(t), \qquad \|\hat{\boldsymbol{\alpha}}(t)\| = 1. \tag{6}$$

Alternative approaches for modeling a low-thrust spacecraft invoke a minimum-fuel formulation, which necessitates the tracking of mass and additional parameterization of the control vector by including both the thrust magnitude and thrust direction [58]. A similar reachable set determination method, proposed by Patel in [51,52,59,60], formulates a minimum-fuel problem and utilizes an inverse mass parameter, $n = 1/m$, to track mass flow. This method resolves some common problems encountered when using standard mass flow dynamics, $\dot{m} = -\|\boldsymbol{T}\|/c$, in that this relation is non-differentiable when $\boldsymbol{T} = \boldsymbol{0}$.

The adopted parameterization of the control vector allows for the thrust vector, $\boldsymbol{T}$, to be linked to the position and velocity states, whereas the thrust magnitude, T_{mag}, is only used to track the change in mass (or inverse mass) of the spacecraft. Most popular implementations of Keplerian motion do not use inverse mass and simply track mass, leading to the dynamics, $\dot{m} = -\|\boldsymbol{T}\|/c$. However, this formulation is non-differentiable when $\boldsymbol{T} = \boldsymbol{0}$, which is eliminated by using n and separating T_{mag}. Two constraints are imposed on the control that simplify the formulation of the reachable set determination problem: the thrust magnitude must be less than the maximum capable by the propulsion system due to power limitations or thruster design considerations. An alternative approach that is convenient for parameterizing the control vector was proposed in Ref. [58].

2.3. Circular Restricted Three-Body Problem (CR3BP)

The reachable set analysis of spacecraft in three-body dynamics has significant utility for near-term cislunar reachability applications. We consider the CR3BP model, which, as demonstrated here, offers more insights into the class of solutions that are obtained. The problem utilizes the rotating synodic frame depicted in Figure 2, where the motion of the two primaries is assumed to be circular and the mass of the third object is negligible. The CR3BP model is normalized such that the distance between the two primaries, the total mass of the system, and the mean motion of the two primary masses are unity. The characteristic length is defined as the distance between the two primaries, l^*; characteristic mass is defined as the sum of the masses of the two primaries, $m^* = m_1 + m_2$; and characteristic time is the mean motion of the primary system, $t^* = \sqrt{l^{*3}/(Gm^*)}$, where G is the universal gravitational constant. In the CR3BP model, the mass ratio is an important parameter used to differentiate between different systems, defined as $\mu = m_2/m^*$. These characteristic values for the Earth–Moon system are as follows [61]: $l^* = 3.844 \times 10^5$ km, $m^* = 6.0458 \times 10^{24}$ kg, $t^* = 375200$ s, and $\mu = 0.0121505856$. Additional terms involving spacecraft mass and thrust must be normalized. Since we assumed the mass of the spacecraft to be negligible from CR3BP first principles, these terms must be normalized by the initial mass of the spacecraft to avoid numerical issues. Since m does not explicitly depend on the state, $\boldsymbol{x}$, we normalize the control accordingly: $m^*_{s/c} = m_{0,s/c}$ and $T^*_{s/c} = m^*_{s/c} l^*/t^{*2}$.

Let $\boldsymbol{r}_1, \boldsymbol{r}_2$, and $\boldsymbol{r} = [x, y, z]^\top$ denote the position vector of the center of mass of the spacecraft from the Earth (m_1), Moon (m_2), and barycenter, respectively. Let $\hat{\boldsymbol{\alpha}} = [\alpha_x, \alpha_y, \alpha_z]^\top$ denote the thrust-steering unit vector.

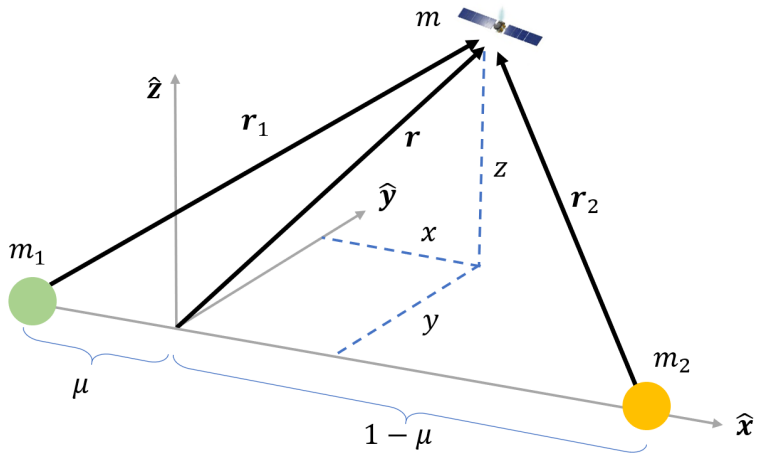

Figure 2. Normalized synodic coordinate system for the CR3BP models.

The equations of motion for a low-thrust spacecraft, expressed in terms of the normalized synodic coordinate system, are

$$\dot{\boldsymbol{x}} = \begin{bmatrix} \dot{\boldsymbol{r}} \\ \dot{\boldsymbol{v}} \end{bmatrix} = \begin{bmatrix} \boldsymbol{v} \\ x + 2v_y - \frac{(1-\mu)(x+\mu)}{r_1^3} + \frac{\mu(x+\mu-1)}{r_2^3} + \frac{T_{\max}}{m}\alpha_x \\ y - 2v_x - \frac{(1-\mu)y}{r_1^3} - \frac{\mu y}{r_2^3} + \frac{T_{\max}}{m}\alpha_y \\ -\frac{(1-\mu)z}{r_1^3} - \frac{\mu z}{r_2^3} + \frac{T_{\max}}{m}\alpha_z \end{bmatrix}, \tag{7}$$

where $r_1 = \sqrt{(x+\mu)^2 + y^2 + z^2}$ and $r_2 = \sqrt{(x+\mu-1)^2 + y^2 + z^2}$ denote the spacecraft distances from the Earth and Moon, respectively.

2.4. Formulation of Minimum-Time Optimal Control Problems

Let Δt denote the stage time interval, where Δt is held constant across all stages. The objective function associated with minimum-time trajectories can be written as

$$\text{minimize} \quad J = \sum_i \Delta t. \tag{8}$$

The Hamiltonian for each stage from the single-stage dynamics, $\boldsymbol{F}^i$; the objective function, J; and the constraint given in Equation (6) can be written as

$$H^i = \Delta t + (\boldsymbol{F}^i)^\top \boldsymbol{\lambda}^{i+1} + \nu_1 \Big(\|\hat{\boldsymbol{\alpha}}^i\| - 1 \Big), \tag{9}$$

where ν_1 is a Lagrange multiplier used to augment thrust constraints to the Hamiltonian. The value of ν_1 must be determined as part of the solution procedure. Let $\boldsymbol{\lambda}^\top = [\boldsymbol{\lambda}_{\boldsymbol{r}}^\top, \boldsymbol{\lambda}_{\boldsymbol{v}}^\top]$ denote the costate vector associated with the states. The costate differential equations are derived by forming the partial derivative of the Hamiltonian in Equation (9) with respect to the state vector, $\boldsymbol{x}$, written as (we use $\boldsymbol{F}_{\boldsymbol{x}}^{i,\top} = (\boldsymbol{F}_{\boldsymbol{x}}^i)^\top$)

$$\boldsymbol{\lambda}^i = \frac{\partial H^i}{\partial \boldsymbol{x}} = H_{\boldsymbol{x}}^i = \boldsymbol{F}_{\boldsymbol{x}}^{i,\top} \boldsymbol{\lambda}^{i+1}. \tag{10}$$

Please note that unlike the continuous-time formulation, there is no negative needed for the $\partial H^i / \partial \boldsymbol{x}$ term. However, Equation (10) is indeed set up to be integrated backward with respect to time since the costate vector from the next stage, $\boldsymbol{\lambda}^{i+1}$, is on the right-hand side. This backward-in-time step is related to the negative sign in $\dot{\boldsymbol{\lambda}} = -[\partial H / \partial \boldsymbol{x}]^\top$

for continuous-time relations obtained from applying the Euler–Lagrange equation in a continuous-time indirect method. The control law is found from the partial derivative of Equation (9) with respect to the control vector, $\boldsymbol{u}$, as

$$\frac{\partial H^i}{\partial \boldsymbol{u}} = H^i_{\boldsymbol{u}} = \mathbf{0} = \boldsymbol{F}^\top_{\boldsymbol{u}} \boldsymbol{\lambda}^{i+1} + \nu_1 \left(\frac{\hat{\boldsymbol{\alpha}}^i}{\|\hat{\boldsymbol{\alpha}}^i\|} \right). \tag{11}$$

In Equations (10) and (11), matrices $\boldsymbol{F_x}$ and $\boldsymbol{F_u}$ denote the state transition and sensitivity matrices, respectively, for linear systems [62]. To evaluate matrices $\boldsymbol{F_x}$ and $\boldsymbol{F_u}$, their matrix differential equations must be propagated through each stage to evaluate their values at the final time of each stage. Let $\Phi = \boldsymbol{F_x}$ and $\Omega = \boldsymbol{F_u}$, and their matrix differential equations [62] can be written as

$$\dot{\Phi}(t, t_i) = \mathbb{A}(t)\Phi(t, t_i), \qquad \dot{\Omega}(t, t_i) = \mathbb{A}(t)\Omega(t, t_i) + \mathbb{C}(t), \tag{12}$$

where the matrices $\mathbb{A}(t) \in \mathbb{R}^{n_x \times n_x}$ and $\mathbb{C}(t) \in \mathbb{R}^{n_x \times n_u}$ can be derived as

$$\mathbb{A}(t) = \frac{\partial \dot{\boldsymbol{x}}}{\partial \boldsymbol{x}} = \begin{bmatrix} \mathbf{0} & \boldsymbol{I} \\ \frac{\partial \dot{v}}{\partial \boldsymbol{r}} & \mathbf{0} \end{bmatrix}, \qquad \mathbb{C}(t) = \frac{\partial \dot{\boldsymbol{x}}}{\partial \boldsymbol{u}} = \begin{bmatrix} \mathbf{0} \\ \mathrm{diag}(\frac{T_{\max}}{m}) \end{bmatrix}. \tag{13}$$

The IMF notation can be updated, and we can rewrite Equation (12) in an integral form as

$$\begin{aligned} \boldsymbol{F}^i_{\boldsymbol{x}} &= \frac{\partial \boldsymbol{x}^{i+1}}{\partial \boldsymbol{x}^i} = \Phi\left(t^{i+1}, t^i\right) = \int_{t^i}^{t^{i+1}} \mathbb{A}(t)\Phi\left(t, t^i\right) dt, \\ \boldsymbol{F}^i_{\boldsymbol{u}} &= \frac{\partial \boldsymbol{x}^{i+1}}{\partial \boldsymbol{u}^i} = \Omega\left(t^{i+1}, t^i\right) = \int_{t^i}^{t^{i+1}} [\mathbb{A}(t)\Omega\left(t, t^i\right) + \mathbb{C}(t)] dt, \end{aligned} \tag{14}$$

with the initial conditions defined as $\Phi(t^i, t^i) = \boldsymbol{I}$ and $\Omega(t^i, t^i) = \mathbf{0}$ (with $\boldsymbol{I}$ denoting the $n_x \times n_x$ identity matrix). The final step of the IMF is to solve Equation (11) for an optimal control law. Applying the strong form of optimality, such that Equation (11) is equal to zero, leads to (since $\|\hat{\boldsymbol{\alpha}}^i\| = 1$)

$$\mathbf{0} = \boldsymbol{F}^\top_{\boldsymbol{u}} \boldsymbol{\lambda}^{i+1} + \nu_1 \frac{\hat{\boldsymbol{\alpha}}^i}{\|\hat{\boldsymbol{\alpha}}^i\|}, \rightarrow -\frac{\boldsymbol{F}^\top_{\boldsymbol{u}} \boldsymbol{\lambda}^{i+1}}{\nu_1} = \frac{\hat{\boldsymbol{\alpha}}^i}{\|\hat{\boldsymbol{\alpha}}^i\|} = \hat{\boldsymbol{\alpha}}^i. \tag{15}$$

Using the definition of $\hat{\boldsymbol{\alpha}}$, ν_1 must be equal to $||\boldsymbol{F}^\top_{\boldsymbol{u}} \boldsymbol{\lambda}^{i+1}||$, which yields the familiar primer vector optimal control law,

$$\hat{\boldsymbol{\alpha}}^i = -\frac{\boldsymbol{F}^{i,\top}_{\boldsymbol{u}} \boldsymbol{\lambda}^{i+1}}{\left\| \boldsymbol{F}^{i,\top}_{\boldsymbol{u}} \boldsymbol{\lambda}^{i+1} \right\|}. \tag{16}$$

An immediate observation is that the optimal control, given in Equation (16), and the costate update map, given in Equation (10), are homogeneous in costates, i.e., multiplying their values by a constant positive factor (e.g., $a > 0$) does not change the solution. The homogeneity property is often used for normalizing the range of the costates (e.g., see Section 10.6 in [63]). We use the homogeneity property of the costate differential equations and the optimal control law in the proposed sampling-based algorithm outlined in Section 3.

2.5. Incorporating Uncertainties in Initial Boundary Conditions

The IMF allows for imposing constraints on only one stage or even using a different cost function across different stages. We take advantage of this feature to incorporate position and velocity ellipsoid uncertainty constraints (per the method of [44]), as well as an impulse maneuver at the simulation start time, adapting the work presented in [52,60].

However, we present numerical results related to the Earth-to-Mars problem. To accomplish this, we add a pseudo-zero stage that converts the reference trajectory initial states, $\boldsymbol{r}^{\text{ref}}$ and $\boldsymbol{v}^{\text{ref}}$, into perturbed initial states, $\boldsymbol{r}^*$ and $\boldsymbol{v}^*$. We use a matrix-mapping technique to account for the variation in each of the states as,

$$\begin{bmatrix} \boldsymbol{r}^* \\ \boldsymbol{v}^* \end{bmatrix} = \begin{bmatrix} \boldsymbol{r}^{\text{ref}} \\ \boldsymbol{v}^{\text{ref}} \end{bmatrix} + \begin{bmatrix} \boldsymbol{I} & \boldsymbol{0} & \boldsymbol{0} \\ \boldsymbol{0} & \boldsymbol{I} & \boldsymbol{I} \end{bmatrix} \begin{bmatrix} \delta\boldsymbol{r} \\ \delta\boldsymbol{v_1} \\ \delta\boldsymbol{v_2} \end{bmatrix}. \tag{17}$$

Our goal is to solve for $[\delta\boldsymbol{r}, \delta\boldsymbol{v_1}, \delta\boldsymbol{v_2}]^\top$, which are the states associated with the variations from the reference state. In Equation (17), $\delta\boldsymbol{r}$ and $\delta\boldsymbol{v_1}$ are associated with ellipsoid position and velocity uncertainty constraints. In addition, ΔV impulse maneuver constraints are handled through $\delta\boldsymbol{v_2}$. An additional cost function is required to account for the variation in initial mass due to the impulse maneuver. We select the Tsiolkovsky rocket equation as the cost function to track the mass consumed due to this impulsive maneuver, defined as $L^* = m_0 - m_0 e^{-\frac{\Delta V}{c}}$. The (pseudo-zero stage) Hamiltonian is formed as

$$H^* = m_0 - m_0 e^{-\frac{\Delta V}{c}} + \boldsymbol{\lambda}^\top [\boldsymbol{r}^{*\top}, \boldsymbol{v}^{*\top}]^\top + \sum_k \nu_k C_k. \tag{18}$$

Next, we must express C_k for both types of constraints. We use the ellipsoid uncertainty constraint formulations from [44] to express the position and velocity uncertainty in the form of equality constraints as

$$\frac{1}{2}\delta\boldsymbol{r}^\top \mathbb{E}_{\boldsymbol{r}} \delta\boldsymbol{r} - \frac{1}{2} r_{\text{ref}}^2 = 0, \qquad \frac{1}{2}\delta\boldsymbol{v_1}^\top \mathbb{E}_{\boldsymbol{v}} \delta\boldsymbol{v_1} - \frac{1}{2} v_{\text{ref}}^2 = 0, \tag{19}$$

where $\mathbb{E}_{\boldsymbol{r}}$ and $\mathbb{E}_{\boldsymbol{v}}$ are matrices determining the major axes of the uncertainty ellipsoid. We need expressions for $\delta\boldsymbol{r}$ and $\delta\boldsymbol{v_1}$ to successfully implement the constraints in Equation (19). Computing the partial derivative of H^* with respect to $\delta\boldsymbol{r}$ yields

$$\frac{\partial H^*}{\partial \delta\boldsymbol{r}} = H^*_{\delta\boldsymbol{r}} = \boldsymbol{0} = \boldsymbol{\lambda_r} + \nu_1 \mathbb{E}_{\boldsymbol{r}} \delta\boldsymbol{r}, \rightarrow \delta\boldsymbol{r} = -(\nu_1 \mathbb{E}_{\boldsymbol{r}})^{-1} \boldsymbol{\lambda_r}, \tag{20}$$

where $\boldsymbol{\lambda_r}$ is the pseudo-zero stage costates associated with the position vector. Substituting Equation (20) into the position ellipsoid constraint, Equation (19), yields an expression for ν_1, which can be written as

$$0 = \frac{1}{2} r_{\text{ref}}^2 - \frac{1}{2} \frac{\boldsymbol{\lambda_r}^\top \mathbb{E}_{\boldsymbol{r}}^{-1} \boldsymbol{\lambda_r}}{\nu_1^2}, \rightarrow \nu_1 = \frac{\boldsymbol{\lambda_r}^\top \mathbb{E}_{\boldsymbol{r}}^{-1} \boldsymbol{\lambda_r}}{r_{\text{ref}}^2}. \tag{21}$$

Substituting v_1 into Equation (20) yields the final equation as

$$\delta\boldsymbol{r} = -r_{\text{ref}} \frac{\mathbb{E}_{\boldsymbol{r}}^{-1} \boldsymbol{\lambda_r}}{\sqrt{\boldsymbol{\lambda_r}^\top \mathbb{E}_{\boldsymbol{r}}^{-1} \boldsymbol{\lambda_r}}}. \tag{22}$$

All parameters in Equation (22) are given, aided by the backward integration in the second stage of the algorithm, which yields the costates, $\boldsymbol{\lambda_r}$. The initial condition position uncertainty constraint can be implemented. It is possible to follow the same process to obtain a solution for $\delta\boldsymbol{v_1}$ as

$$H^*_{\delta\boldsymbol{v_1}} = \boldsymbol{0} = \boldsymbol{\lambda_v} + \nu_2 \mathbb{E}_{\boldsymbol{v}} \delta\boldsymbol{v_1}, \qquad \delta\boldsymbol{v_1} = -v_{\text{ref}} \frac{\mathbb{E}_{\boldsymbol{v}}^{-1} \boldsymbol{\lambda_v}}{\sqrt{\boldsymbol{\lambda_v}^\top \mathbb{E}_{\boldsymbol{v}}^{-1} \boldsymbol{\lambda_v}}}. \tag{23}$$

Equations (22) and (23) are analytical closed-form expressions for the change in initial conditions due to an ellipsoid uncertainty. These changes can be implemented in the reach-

able set algorithm without any structural modification to the algorithm (see Equation (17)). The other type of scenario is the ΔV impulse maneuver, which involves a separate boundary condition since one must allow the magnitude of the ΔV impulse to take values less than or equal to the maximum capability of the propulsion system, $\Delta V_{\max}$. This constraint associated with the initial impulse can be written as

$$\frac{1}{2}\delta \boldsymbol{v_2}^\top \delta \boldsymbol{v_2} - \frac{1}{2}\Delta V_{\max}^2 \leq 0. \tag{24}$$

The derivation of the closed-form solutions for these constraints is more involved due to the introduction of an inequality constraint that can be active or inactive. A complete derivation of the solution for $\delta \boldsymbol{v_2}$ and ΔV is given in Appendix A. However, if the inequality constraint is active, we have the following two relations

$$\Delta V = \Delta V_{\max}, \qquad \delta \boldsymbol{v_2} = -\Delta V_{\max} \frac{\boldsymbol{\lambda_v}}{\|\boldsymbol{\lambda_v}\|}. \tag{25}$$

If the inequality constraint is not active, the optimal solution can be derived as

$$\Delta V = -c \ln\left(\frac{\|\boldsymbol{\lambda_v}\|c + \sqrt{\|\boldsymbol{\lambda_v}\|^2 c^2}}{2m_0}\right), \quad \delta \boldsymbol{v_2} = c \ln\left(\frac{\|\boldsymbol{\lambda_v}\|c + \sqrt{\|\boldsymbol{\lambda_v}\|^2 c^2}}{2m_0}\right) \frac{\lambda_v}{\|\boldsymbol{\lambda_v}\|}. \tag{26}$$

The final step is to address the initial mass perturbation due to an impulse maneuver, which can be written as $\delta m = m_0 - m_0 e^{-\frac{\Delta V}{c}}$, with ΔV becoming the computed value using the logic presented above. Finally, we need to update the initial mass as $m^* = m_0 + \delta m$. We emphasize that the analytical solutions (for an initial condition variation due to an impulse maneuver) are only functions of the costates and other constants specified by the problem. This makes the implementation of these types of constraints simple given the algorithm structure (i.e., treating stages differently).

3. Reachable Set Approximation Algorithm

The rapid reachable set approximation algorithm consists of three main phases. First, a zero-thrust reference trajectory is used to obtain all reference states, state transition matrices, and sensitivity matrices. Second, a sufficiently large number of costates (at the final stage, N) are sampled from a six-dimensional unit ball corresponding to the costates associated with the position and velocity vectors. It is at this stage that the homogeneity property of the costate differential equations is leveraged. For each sampled costate vector, the costate vectors are propagated backward in time using the costate update mapping in Equation (10) until the initial stage. Control laws, given by Equation (16), are computed and stored. Lastly, the reachable set is reconstructed using a forward-in-time integration of the fully *nonlinear* state dynamics with the computed optimal control. The sampling-based aspect of the algorithm allows for thousands of reachable trajectories to be generated rapidly and in a parallel manner. Note that for each trajectory, there is only one numerical integration, and no optimization solver is used (as opposed to a direct optimal control method).

To generate a reference trajectory, we consider a zero-thrust (i.e., ballistic) trajectory. This is due to a trivial solution of the OCP in which $\boldsymbol{\lambda}^N = \mathbf{0}$, causing $\{\boldsymbol{u}_i\}_{i=1}^N = \mathbf{0}$. The system dynamics are forward-in-time integrated from the initial conditions, $\boldsymbol{x}^0$, with no control to obtain the reference trajectory, $\boldsymbol{x}^{\text{ref}}$, and matrices $\{\boldsymbol{F_x}^i\}_{i=1}^N$ and $\{\boldsymbol{F_u}^i\}_{i=1}^N$. Next, we sample terminal stage costates, $\boldsymbol{\lambda}^N$, from a six-dimensional unit ball (i.e., $\left\|\boldsymbol{\lambda}^N\right\| = 1$). The reason we uniformly sample $\boldsymbol{\lambda}^N$ is due to the control law in Equation (16), which indicates that the magnitude of $\boldsymbol{\lambda}^N$ does not matter (the control law is homogeneous in costates); hence, a reasonable method to determine these values is to uniformly sample them from a unit ball. The proper sampling algorithm is provided in Appendix A. All previous stage costates are recovered backward in time through a recursive matrix multiplication, as

outlined in Equation (10). The optimal control can be computed using Equation (16), and a final forward-in-time integration is used to produce the entire reachable set. The indices i and j in Figure 3 indicate the i-th stage variable quantity and the j-th trajectory forming the reachable set. The reachable set approximation algorithm is outlined in Algorithm 1.

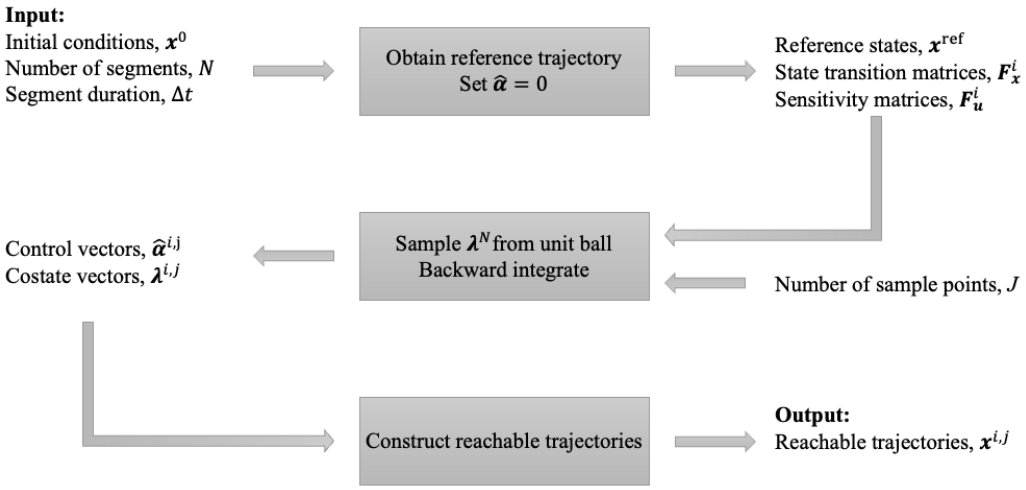

Figure 3. Flowchart for the reachable set approximation algorithm.

Note that $(-\boldsymbol{F}_{\boldsymbol{u}}^{i,\top}\boldsymbol{\lambda}^{i+1})$ denotes the primer vector since Pontryagin's minimum principle is used to minimize the Hamiltonian. The proposed algorithm shares multiple aspects with a recent minimum-time-based algorithm by Patel [60], but we briefly discuss some key differences between the method dubbed "FFOE" and our proposed algorithm. First, FFOE utilizes a cost function designed to maximize the final state in a unit-ball sampled direction, whereas our proposed method formulates a minimum-time IMF problem that allows direct comparison with the solution to a minimum-time OCP. Additionally, our formulation simplifies the dynamics by removing mass and its costate differential equations from the set of state–costate vectors. This is aided by the minimum-time formation since it is known that mass can be integrated analytically using the thrust value, specific impulse value, and time of flight [57]. Ref. [60] tracked the inverse of mass, which increased the dimensionality of both the differential equations and the involved matrices, leading to a longer computational time compared to our proposed algorithm. The computational advantage of our proposed method remains valid and is independent of the computational platform and programming language.

Nevertheless, we can use the combined observations from this study and [60] to draw conclusions on a few salient aspects of the sampling-based reachable set estimation method. In general, the algorithm's accuracy begins to deteriorate over long time horizons *unless* the number of sample points increases. Additionally, since the core of this method involves linearization about an unpowered reference trajectory, we expect that as the ratio of the propulsive acceleration to the natural acceleration due to the gravity of the gravitational body(s) increases, the accuracy of the reachable set algorithm will decrease.

These issues were also identified in [60], in which FFOE was used in an iterative manner. In this approach, each sample trajectory was linearized, and the reachable set was recomputed. However, the method exhibited diminishing returns and numerical stability issues. For the Earth-to-Mars problem [64], the results indicate that for the two-body problems, the number of samples does not have to be large. The presented numerical results for the CR3BP model indicate that accurate and rapid approximation of reachable sets is possible with a sufficiently large sample of points, in particular, over relatively short time horizons, which are practical for reachable set approximation of low-thrust spacecraft.

Algorithm 1: Reachable set determination

Result: $\boldsymbol{x}^{i,j}$ Reachable Trajectories
$\boldsymbol{x}^0 \leftarrow$ Initial Conditions;
$\boldsymbol{p} \leftarrow$ Constant Parameters;
$N \leftarrow$ Number of Segments;
$\Delta t \leftarrow$ Segment Duration;
$J \leftarrow$Number of sampled reachable points;
$\boldsymbol{u}^{\text{ref}} \leftarrow \mathbf{0}$;
$t^i \leftarrow 0$;
while $i = 0; i < N; i \leftarrow i + 1$ **do**
  $\boldsymbol{x}^{i+1}, \boldsymbol{F}_{\boldsymbol{x}}^i, \boldsymbol{F}_{\boldsymbol{u}}^i \leftarrow \boldsymbol{F}^i\left(\boldsymbol{x}^i, \boldsymbol{u}^{\text{ref}}, t^i, t^i + \Delta t; \boldsymbol{p}\right)$; `/* Unpowered ref trajectory */`
  $\boldsymbol{x}^i \leftarrow \boldsymbol{x}^{i+1}$;
  $t^i \leftarrow t^i + \Delta t$;
end
for $j = 1 : J$ **do**
  $\boldsymbol{\lambda}^{N,j} \leftarrow$ Sampled from a unit 6-D ball (i.e., $||\boldsymbol{\lambda}^{N,j}|| = 1$);
  $i \leftarrow N$;
  while $i = N; i \geq 1; i \leftarrow i - 1$ **do**
    $\hat{\boldsymbol{\alpha}}^{i,j} \leftarrow -\frac{\boldsymbol{F}_{\boldsymbol{u}}^{i,\top} \boldsymbol{\lambda}^{i+1,j}}{\left\| \boldsymbol{F}_{\boldsymbol{u}}^{i,\top} \boldsymbol{\lambda}^{i+1,j} \right\|}$; `/* Optimal unit thrust steering vector */`
    $\boldsymbol{\lambda}^{i,j} \leftarrow \boldsymbol{F}_{\boldsymbol{x}}^{i^\top} \boldsymbol{\lambda}^{i+1,j}$;
  end
end
for $j = 1 : J$ **do**
  while $i = 0; i < N, i \leftarrow i + 1$ **do**
    $\boldsymbol{x}^{i+1} \leftarrow \boldsymbol{F}^i\left(\boldsymbol{x}^i, \hat{\boldsymbol{\alpha}}^{i,j}, t^i, t^i + \Delta t; \boldsymbol{p}\right)$; `/* Reachable trajectories */`
    $\boldsymbol{x}^i \leftarrow \boldsymbol{x}^{i+1}$;
    $t^i \leftarrow t^i + \Delta t$;
  end
  $j \leftarrow j + 1$;
end

4. Two-Body Dynamics Results

The results obtained for the rapid reachability and rendezvous determination problem for a minimum-time Earth-to-Mars transfer are presented in this section. This example was taken from [65]. For all results, $T_{\max} = 0.5$ Newton, $I_{\text{sp}} = 3000$ s, and $m_0 = 1000$ kg. The initial position and velocity vectors are $\boldsymbol{r} = [-140699693; -51614428; 980]^\top$ km and $\boldsymbol{v} = [9.774596; -28.07828; 4.337725\text{E-}4]^\top$ km/s, respectively. The complete state vector of the spacecraft at the beginning of the maneuver is given as $\boldsymbol{x} = [-140699693; -51614428; 980; 9.774596; -28.07828; 4.337725\text{E-}4]^\top$, with units km and km/s corresponding to a departure epoch of 10 April 2007. The segment duration, Δt, is set to 86,400 s. The reachable set algorithm was implemented in MATLAB R2023a on a 2018 MacBook Pro with a quad-core 2.3 GHz processor, using parallel computing capabilities with 4 CPU cores. Additionally, MATLAB's integrated code compiler was used to generate MEX files to speed up the algorithm. NASA's spice toolkit was used to access DE440 planetary ephemerides. The computations were completed in the J2000 ecliptic reference frame, centered at the solar system barycenter.

4.1. Reachable Set Analysis for a Fixed Time Horizon

We consider a time horizon of 200 days with a total of 5000 sample trajectories. This simulation completed in 13.61 s, demonstrating rapid trajectory generation ability with

2.72 ms per trajectory. The first, and most important, observation from Figure 4a is that for the time horizon of 200 days, a portion of the Mars orbit is within the reachable set. However, the position of Mars (red square) is not within the reachable set (red). A longer time of flight is required for Mars to become reachable. The reference trajectory (blue line) is equivalent to the orbit of the Earth, since no control is applied. In Figure 4a, AU stands for the astronomical unit (AU = 149×10^6 km).

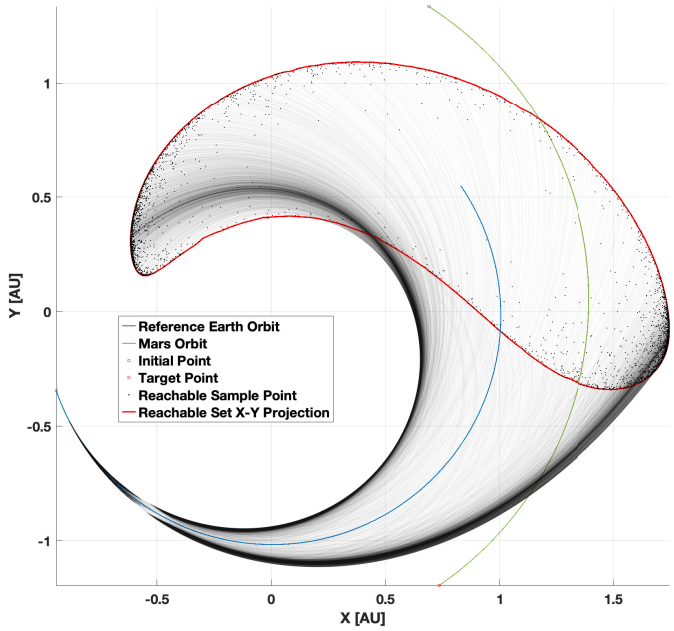

(**a**) Two-dimensional view of the position reachable set

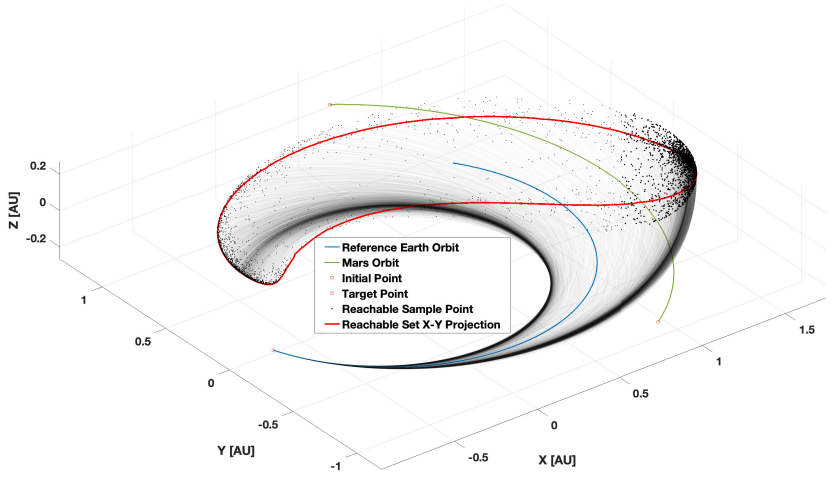

(**b**) Three-dimensional view of the position reachable set

Figure 4. Position reachable set over a 200-day time horizon with 5000 sample trajectories.

Figure 4b depicts a three-dimensional (3D) view of the reachable set, which is a deformed ellipsoid-like 3D shape created by the endpoint of all reachable trajectories. A funnel-like structure exists when we plot the time history of all reachable trajectories (light gray lines); we refer to this as the reachable funnel. The boundary points of the reachable funnel represent the time history of all reachable sets within a 200-day time horizon. The feasible set and feasible funnel encompass all position states classified as the interior of the reachable set and reachable funnel, corresponding to minimum-fuel solutions for the fixed time horizon. As the time of flight increases, the number of sample trajectories has to be increased because for long-time-horizon maneuvers, the volume of the reachable set

expands rapidly, so more sample points are required to construct an accurate approximation of the reachable set.

4.2. Reachable Set Comparison with the Solution from a Direct Optimization Formulation

We seek to validate the accuracy of the reachable set estimate by comparing the results in Section 4.1 with a minimum-time trajectory optimization problem, as minimum-time trajectories lie on the boundary of the reachable set. We solve a minimum-time direct OCP with the same initial conditions listed above. The minimum-time Earth-to-Mars OCP was solved using CasADi v3.5.5 [66]) ; the resulting optimal trajectory and thrust vector are shown in Figure 5. It can be observed that the propulsion system operates at maximum thrust for the duration of the flight, with only the thrust direction (red arrows) in Figure 5 varying. The minimum-time Earth-to-Mars problem, when solved, resulted in a trajectory with a time of flight of 307 days. The trajectory also leveraged the Oberth effect (i.e., it utilized the gravitational well of the Sun to maximize the rate of change of its energy). Taheri posed a minimum-fuel Earth-to-Mars problem in [65] and described how a (Hamiltonian) two-point boundary-value problem arises from an indirect formulation, which can be solved with a single-shooting method (e.g., using MATLAB's built-in `fsolve` function). We used this same formulation and manually iterated on the time of flight until a trajectory was determined that produced a constant maximum thrust profile in the shortest time of flight. The same solution can also be obtained by formulating a minimum-time OCP and using an NLP solver (e.g., CasADi v3.5.5 [66]).

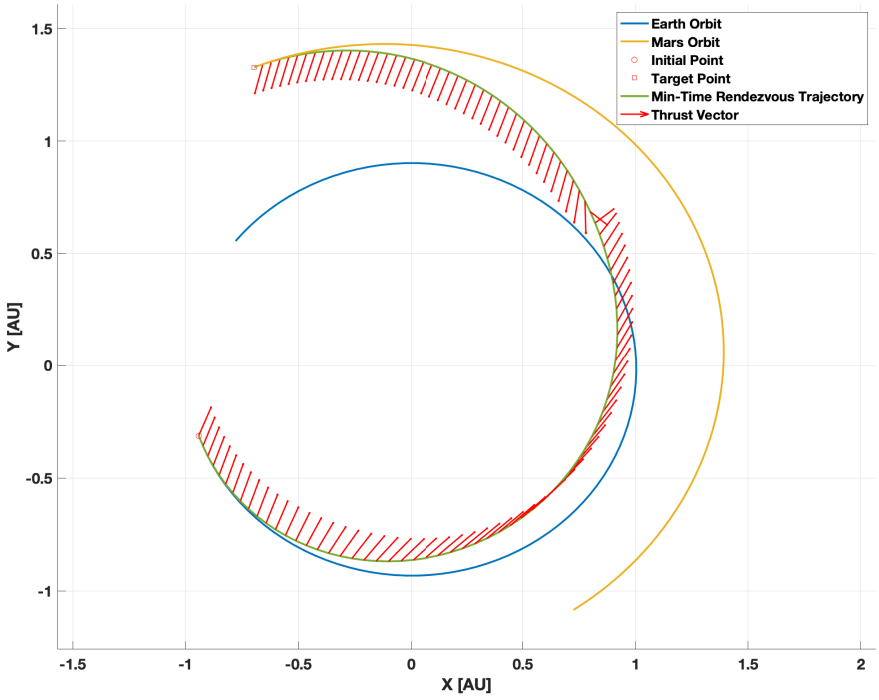

Figure 5. Minimum-time trajectory and thrust vector solved with CasaDi.

The solution of the minimum-time Earth-to-Mars problem aligns with ephemeris-consistent rendezvous boundary conditions (i.e., when the position and velocity of Mars depend on the time of flight). The resulting minimum-time trajectory can be used to demonstrate the validity of the reachable set estimations because a minimum-time trajectory, by definition, must terminate on the reachable set. To show this, we computed the reachable position and velocity sets for the time of flight computed by the optimal single-trajectory indirect OCP [57]. Figure 6 shows the evolution of the velocity reachable set through flight times from 120 to 180 days. We selected these times of flight since they correspond to the

thruster direction reversing in Figure 5. The reachable set appears to fold upon itself when chronologically stepping from 140 days (Figure 6b) to 160 days (Figure 6c).

The reachable set algorithm was used to compute the reachable set for a time horizon of 307 days with 5000 sample points. Figure 7a shows the position reachable set for the given initial conditions. Upon examination, we can see that the indirect OCP generates a position-feasible trajectory (green line) due to the fact that in position space, the minimum-time trajectory terminates on the interior of the projected position reachable set. Figure 7b depicts the velocity reachable set. The indirect minimum-time trajectory terminates on the boundary of the velocity reachable set. The results indicate that for the considered parameters of the propulsion system, the velocity states are more restrictive compared to the position set and reduce the combined reachable velocity. Moreover, the results are consistent and validate the accuracy of our proposed method for determining an accurate estimate of the reachable set for low-thrust spacecraft. However, the sensitivity of the reachable set for fixed-time rendezvous maneuvers is more nuanced, as discussed for a rendezvous maneuver from Earth to asteroid 1989ML in [50], which is a consequence of the deformed reachable set within the orbit of asteroid 1989ML.

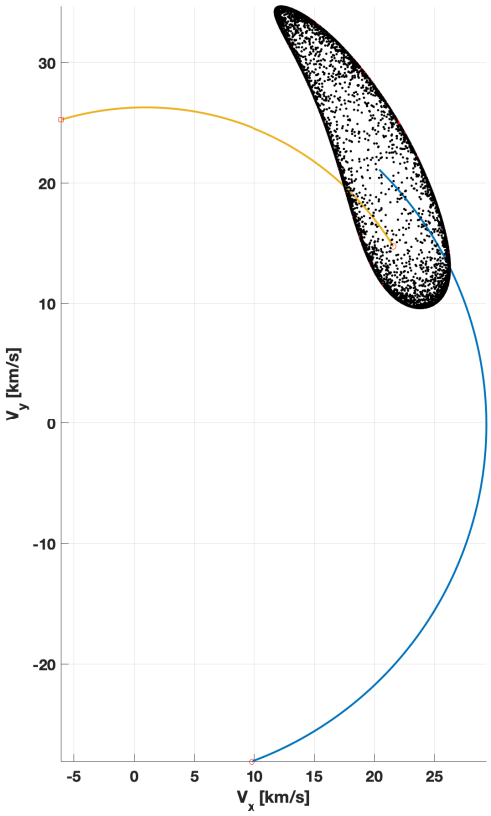

(**a**) Velocity reachable set over 120 days.

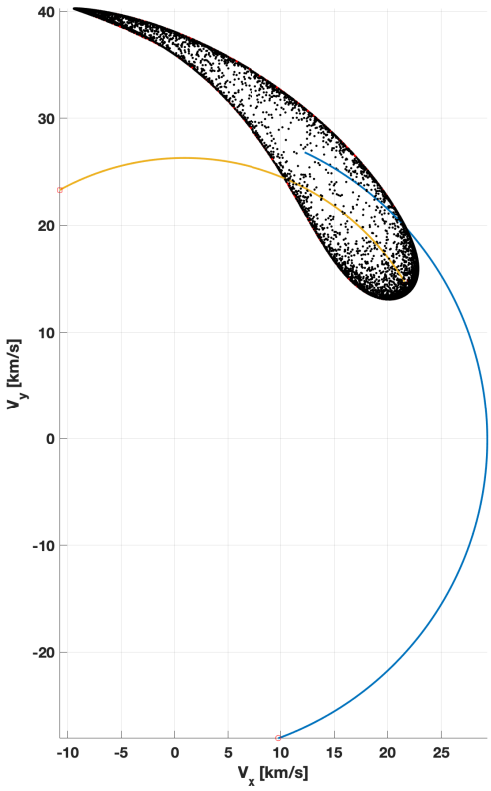

(**b**) Velocity reachable set over 140 days.

Figure 6. *Cont.*

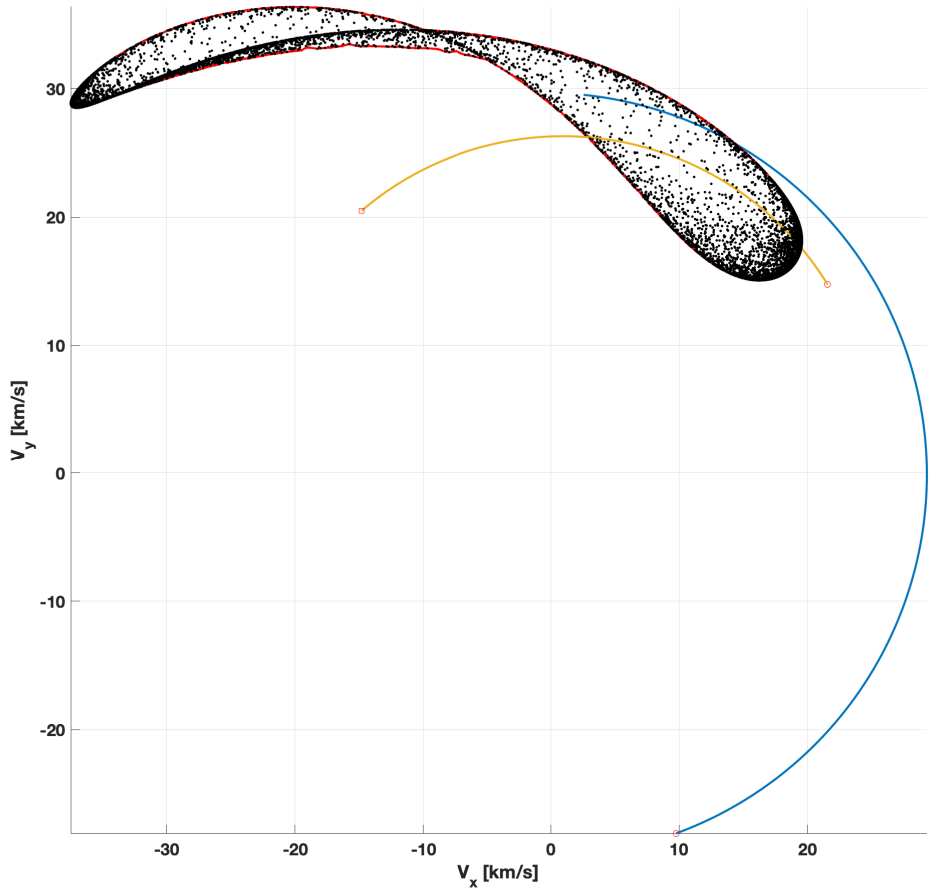

(**c**) Velocity reachable set over 160 days.

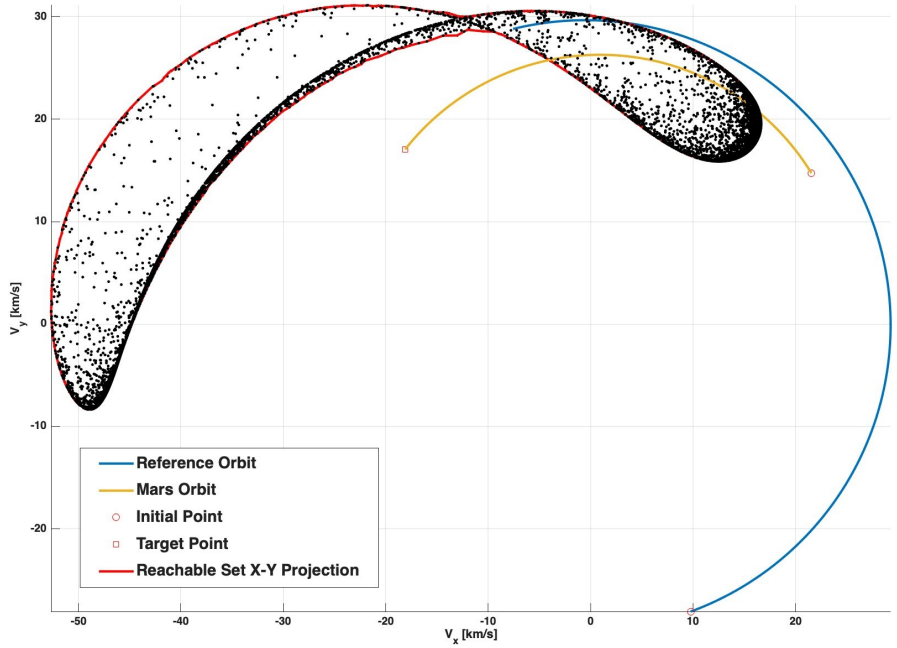

(**d**) Velocity reachable set over 180 days.

Figure 6. Evolution of velocity reachable set vs. different time horizons.

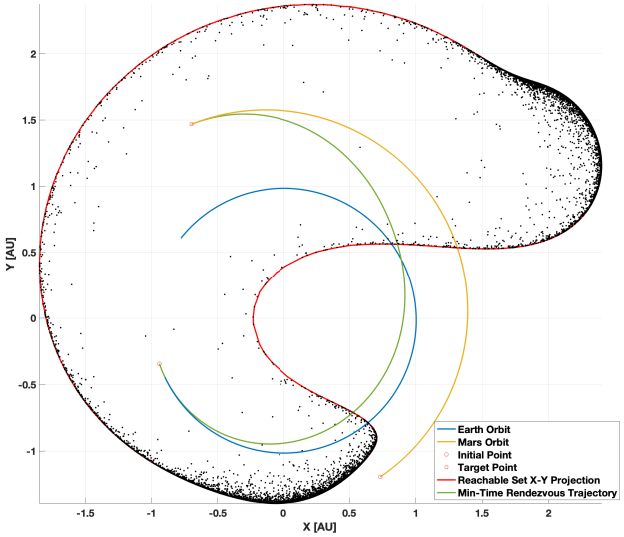

(**a**) Position reachable set over a 307-day time horizon.

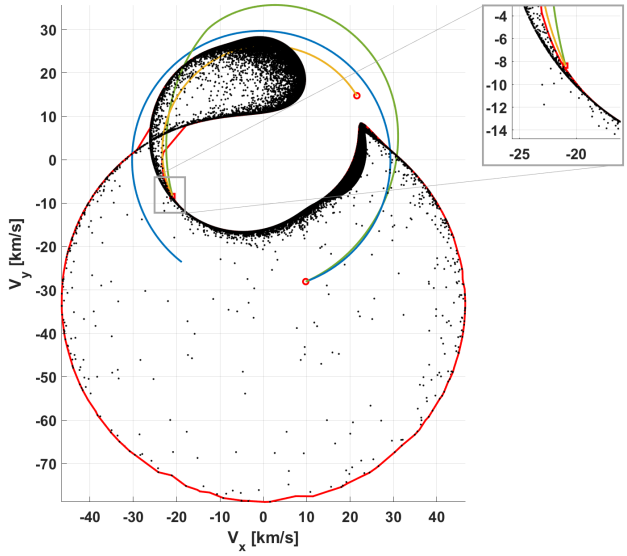

(**b**) Velocity reachable set over a 307-day time horizon.

Figure 7. Reachable set over a 307-day time horizon with 5000 samples.

4.3. Reachable Set Propagation and Analysis of the Required Computation Time

One useful application of the proposed reachable set approximation method is the ability to rapidly determine whether a planet/object can be encountered from given initial conditions within a specified time horizon. To demonstrate this capability, the reachable set algorithm was initialized such that one stage was equal to one day. Then, 10,000 sample trajectories were computed for each trial. Data indicating the time of flight and simulation run times are presented in Table 1. The fast computation time allows for rapid iteration to "brute force" search for a time of flight that allows a target to become reachable.

Figure 8 indicates the expansion of the reachable position set over an increasing time horizon, with flight times ranging from 100 to 300 days. This pseudo-qualitative plot was generated by interpolating all sampled trajectories on the reachable set to graphically illustrate the reachable set. The trajectory of Mars (red line) shows how the target position evolves with increasing time of flight.

Table 1. Earth-to-Mars reachable set propagation with 10,000 sample points.

Time of Flight (days)	Computation Time (seconds)
100	9.0599
150	17.3945
200	18.1148
250	21.8414
300	26.2118

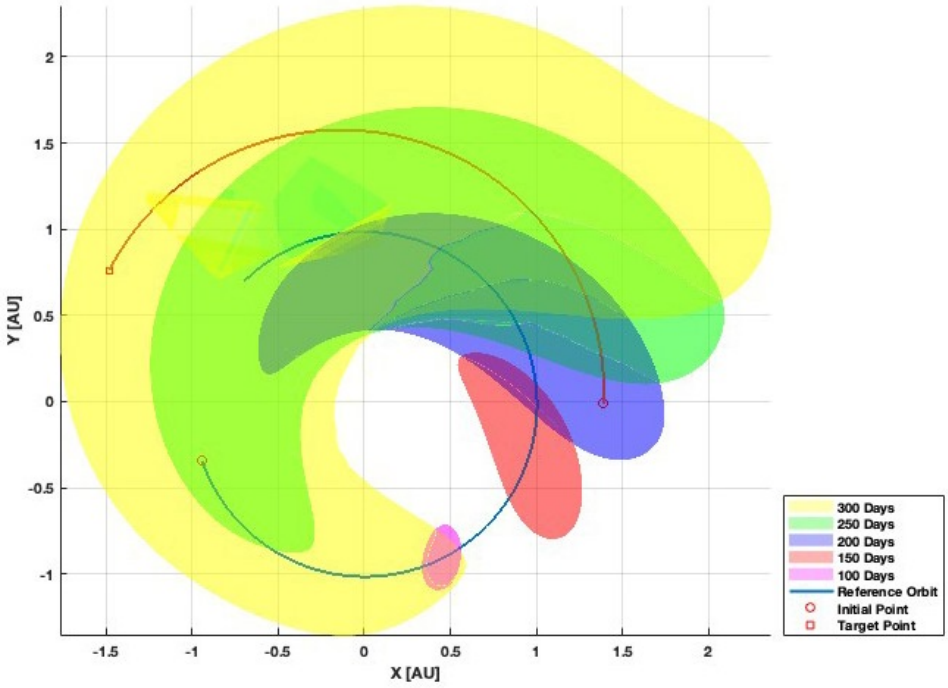

Figure 8. Depiction of the Earth-to-Mars position reachable set.

The utility of the rapid reachable algorithm is illustrated here, since the successive generation of many reachable sets for complex problems is extremely computationally expensive. In Figure 8, we can see that the time of flight must be greater than 250 days for Mars to be reachable. Recall that position reachability is the first step in determining whether an object can be reached in a rendezvous scenario, which confirms the results of the previous section.

4.4. Reachable Set Variations with Uncertainties in Initial Boundary Conditions

We revisit the simulation presented in Section 4.1 to demonstrate the ability to add uncertainties in initial boundary conditions and assess their impact on the reachable set. Two types of initial boundary conditions are considered: (1) position and velocity uncertainty, and (2) a bounded impulsive maneuver. Both types of constraints can be incorporated simultaneously; however, we separate them in these results to demonstrate their individual effects. We consider departure from the Earth (reference) orbit.

Figure 9a shows the reachable set for a case without position and velocity uncertainty (green surface) and a case for ellipsoidal position and velocity (red surface). The addition of ellipsoidal uncertainty constraints clearly affects the nominal reachable set, and it appears that the red set has decreased in size relative to the green set. However, this is not necessarily the case since the uncertainty constraint has also shifted the red reachable set out of the plane relative to the green reachable set, making it appear smaller. The main conclusion

is the demonstration that ellipsoidal uncertainty constraints can significantly affect the reachable set. Figure 9b presents the expected result of adding an initial ΔV impulse (which can be regarded as excess velocity provided by a launch vehicle). The impulse maneuver excites the spacecraft to a higher energy state, which ultimately leads to a larger reachable set. The red set resulting from the impulse maneuver has noticeably expanded after a 200-day time horizon compared to the zero-impulse-maneuver reachable (green) set.

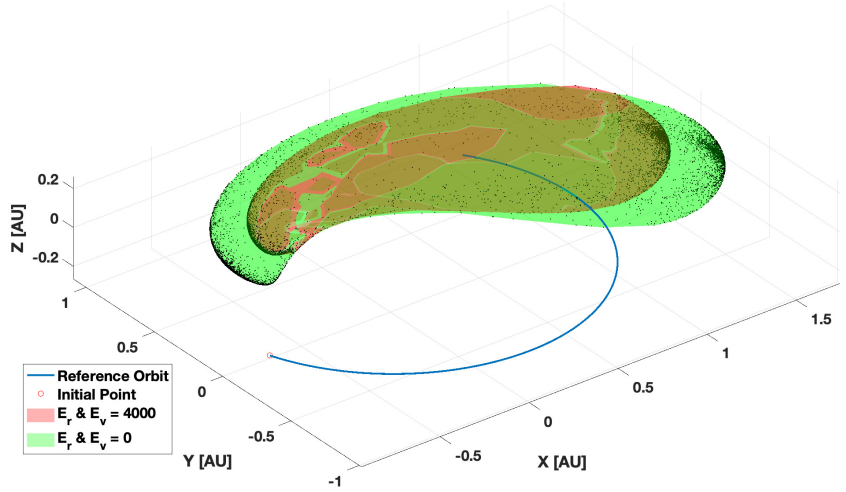

(**a**)

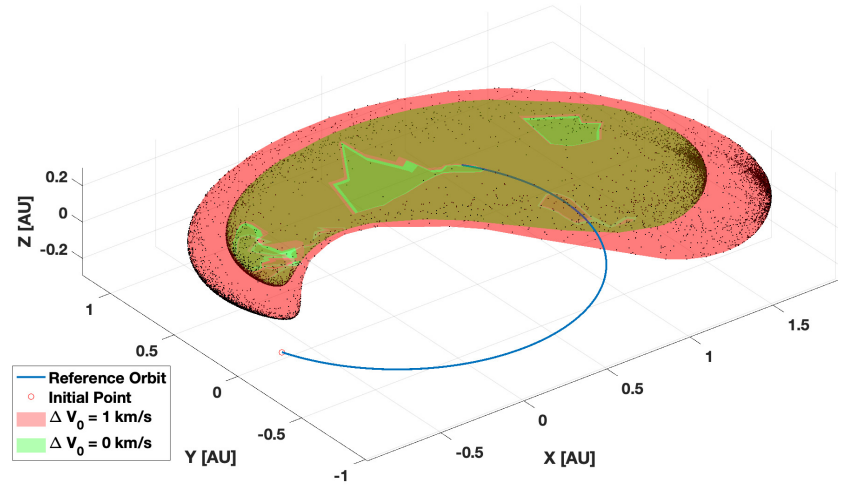

(**b**)

Figure 9. Comparison of position reachable sets over a 200-day time horizon with 5000 samples with different initial types of uncertainties. (**a**) With uncertainties on the initial position and velocity vectors as defined in Equation (19). (**b**) With an initial impulse maneuver as defined in Equations (25) and (26).

5. CR3BP Dynamics Reachable Set Results

Results are presented for three cases, considering different spacecraft propulsion and mass parameters across various time-horizon values. Case 1 starts from an L1 point initial condition with zero velocity and extends over increasing time-horizon values. The results of our algorithm are in agreement with the results presented in [67] for the same problem and parameters. Case 2 simulates an L2 Halo orbit over both short- and long-time-horizon values and illustrates the chaotic natural dynamics and the evolution of the reachable set in the CR3BP dynamics. Case 3 updates the initial condition to a Lunar Gateway 9:2 NRHO, which is the chosen orbit for NASA's Lunar Gateway station [68]. Case 1 serves to validate the reachable set results within the CR3BP dynamics, whereas Cases 2 and 3 present

novel reachable set solutions in cislunar space. Lastly, an explanation involving invariant manifolds is presented to offer additional insights into the evolution of the reachable sets in the CR3BP dynamics. In all results presented, the Earth and Moon are not illustrated to scale, and the segment duration, Δt, was determined empirically as the time of flight normalized by the characteristic time, divided by 200.

5.1. Reachability from the L1 Point (Case 1)

A low-thrust spacecraft with $T_{\max} = 1$ N, $I_{sp} = 2000$ s, and 1500 kg of initial mass is considered. The initial state vector is given in nondimensionalized coordinates as $\boldsymbol{x} = [0.836892919; 0; 0; 0; 0; 0]^\top$. The reachable set was computed for time-horizon values ranging from 50 to 200 h. Each trial used 100,000 sample trajectories. The longest simulation run time, for 200 h, took 119 s. Compared with [67], which is a planar implementation of cislunar CR3BP, Figure 10 utilizes full three-dimensional dynamics. The computational advantage of our proposed method is significant and is expected since the determination of the reachable set using a direct optimization method is computationally demanding.

The sample points that appear to be interior to the reachable set with this $X - Y$ projection are due to the out-of-plane effects and are simply reachable points with a Z-coordinate not equal to zero. The results validate the accuracy of the linearization of the CR3BP dynamics. One interesting result corresponds to the area to the right of the Moon, where the chaotic nature of the CR3BP dynamics results in large discontinuities in the solution. It is suspected that the singularity of the trajectories due to the presence of the Moon gives rise to the chaotic behavior of the reachable set. As is common in constrained trajectory optimization, it is possible to enforce position-level path inequality constraints on the radius vector of the spacecraft to avoid singularities. The tendency of the reachable set to grow toward the Earth is attributed to the CR3BP dynamics, with the influence of the eigenvectors at the L1 diverging toward the Earth corresponding to larger eigenvalues.

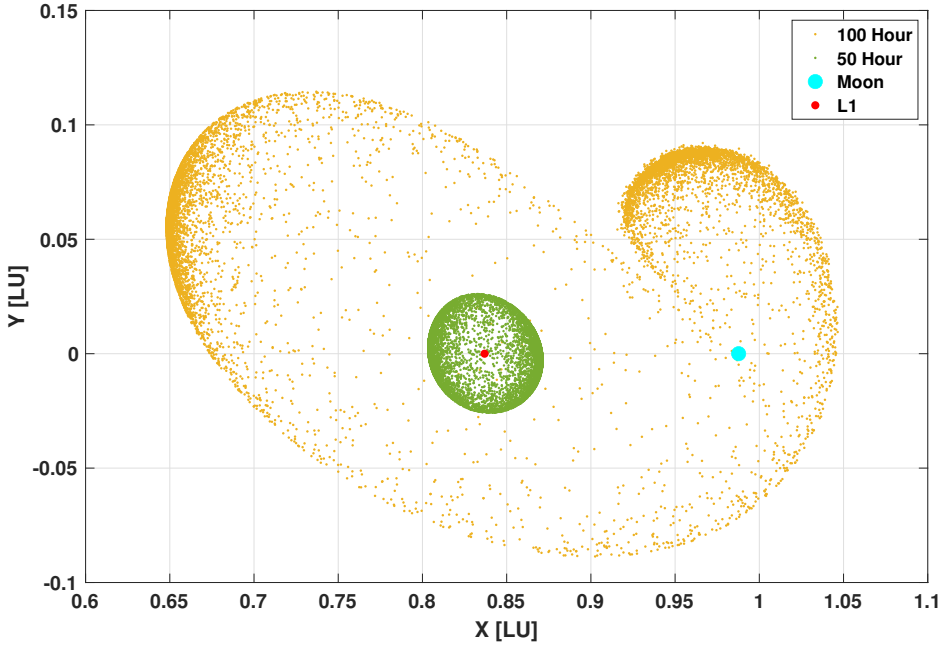

(**a**) 50–100 h time horizon.

Figure 10. *Cont.*

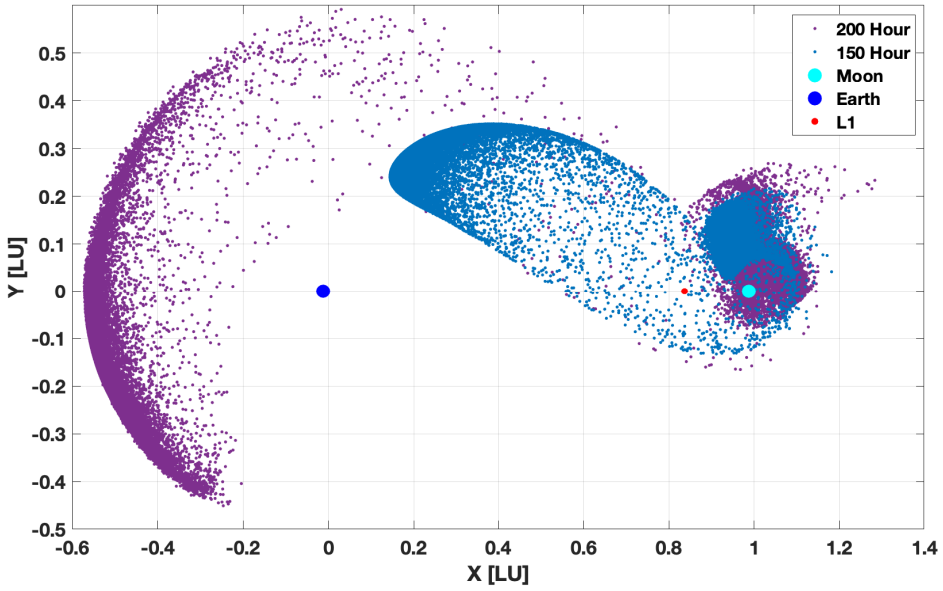

(**b**) 150–200 h time horizon.

Figure 10. L1 point reachable sets with increasing time-horizon values.

5.2. Reachability from the L2 Halo Orbit (Case 2)

Case 2 considers the computation of the reachable set for an L2 Halo orbit. A low-thrust spacecraft with $T_{\max} = 0.2$ N, $I_{sp} = 3000$ s, and $m_0 = 1000$ kg is considered. The initial state vector is given in nondimensionalized coordinates as

$$\boldsymbol{x} = [1.17204419281306; 0; -0.0862093101977581; 0; -0.188009087163036; 0]^{\top}.$$

The period of the L2 reference orbit is 346.322857 h. The reachable set was computed for time-horizon values equal to 150 and 350 h. The 150 h time horizon demonstrates the evolution of the reachable set in the vicinity of the Moon, and the 350 h time horizon shows growth and a distributed reachable set.

Figure 11 shows the 150 h expansion of the reachable set with 2000 sample trajectories. Even on this short time horizon, one can identify that small changes in the thrust vector (especially during the initial stages) directly contribute to a reachable set that is fully developed in three dimensions. Unlike the short time-horizon two-body results in which it is straightforward to interpolate the reachable sample points to generate a reachable set boundary projection, it is difficult to fully capture the shape of the abstract reachable set. Additionally, Figure 11 shows an incipient tendency for the reachable trajectories to cluster into two bands, each propagating in opposite directions from the initial point. This phenomenon is the primary purpose of including the relatively long 350 h time-horizon case and is explained in the section on invariant manifolds.

For the 350 h time-horizon case, the number of sample points was increased to 10,000 to improve the resolution of the captured reachable set. Figure 12 presents the computed reachable set for the L2 Halo reference orbit. These results clearly show that the reachable set has distributed into two primary clusters. One cluster completes a close flyby with the Moon, and the second cluster exits the near vicinity of the Moon into an area dominated by the gravitational attraction of the Earth. The section detailing invariant manifolds outlines the theoretical foundation for why this reachable set is deformed in such a manner and why the uniformly sampled trajectories exhibit unexpected clustering behavior.

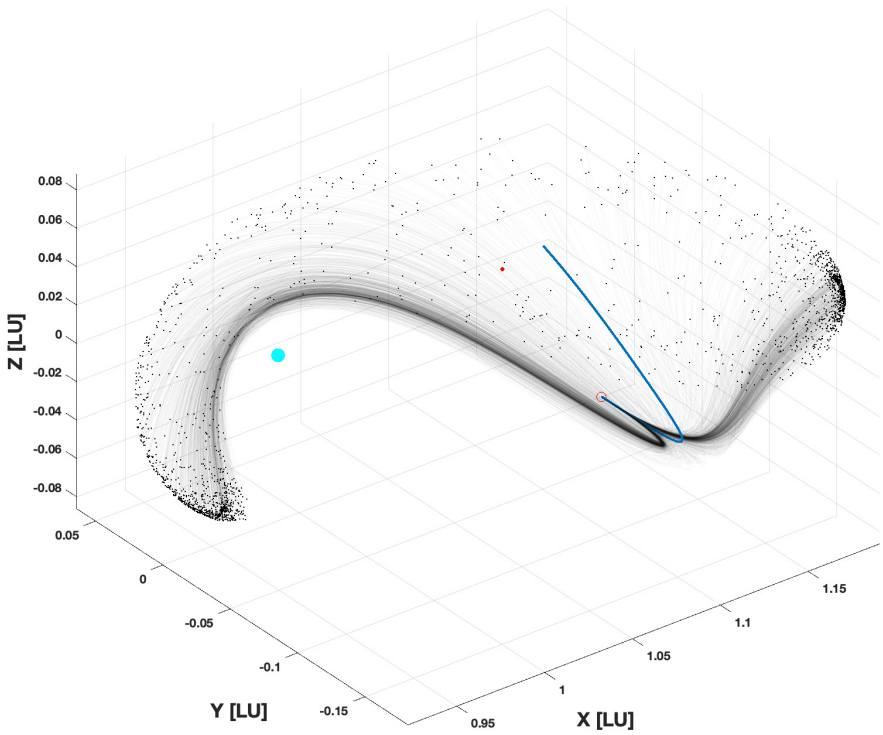

(**a**) Three−dimensional view of the position reachable set.

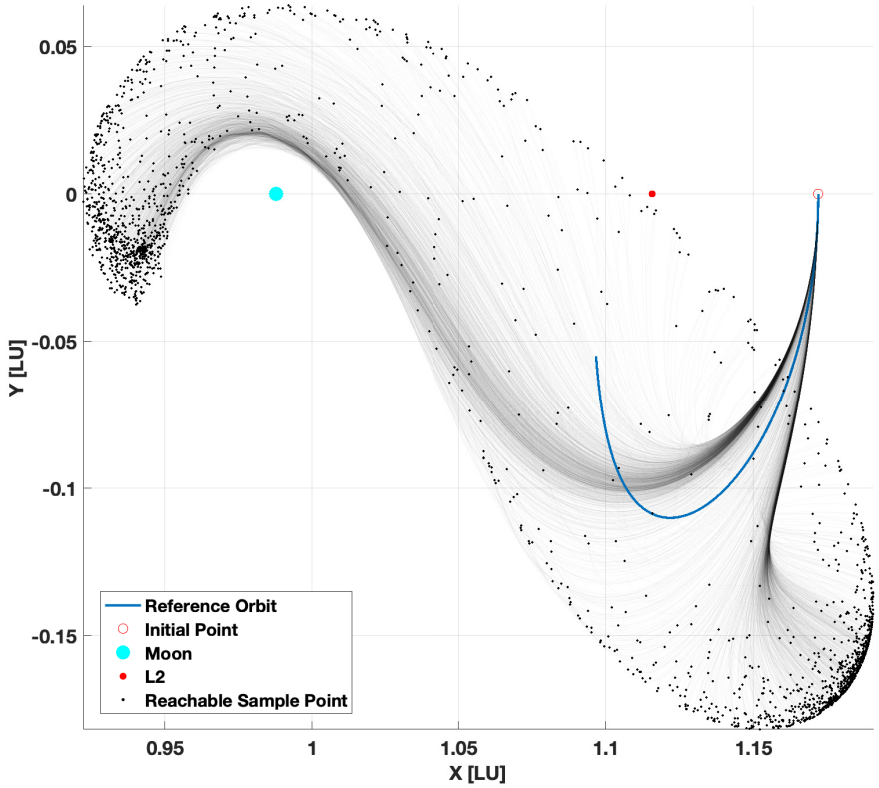

(**b**) XY view of the position reachable set.

Figure 11. Position reachable set over a 150 h (6.25 days) time horizon with 2000 samples.

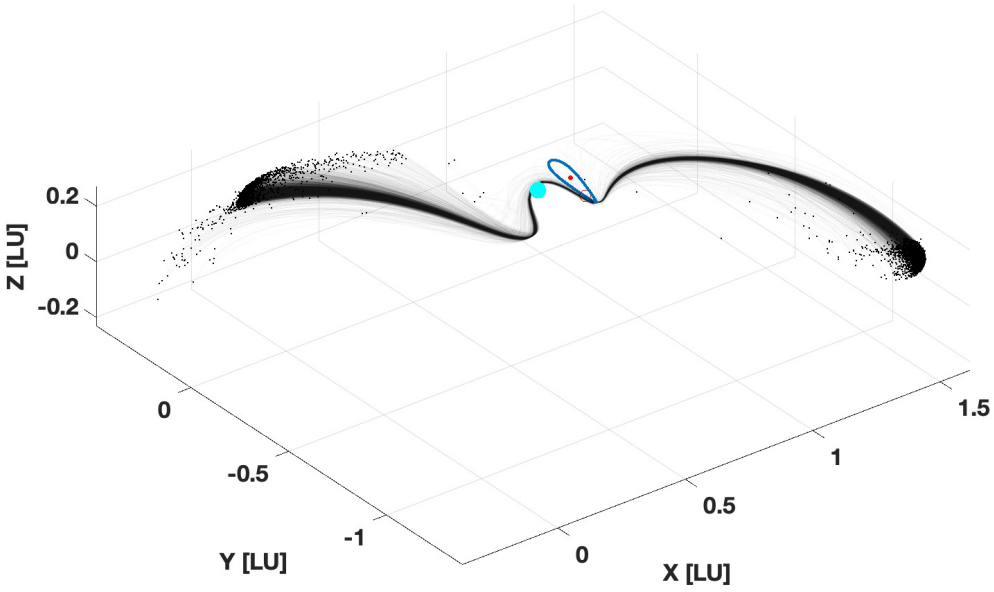

(**a**) Three-dimensional view of the position reachable set.

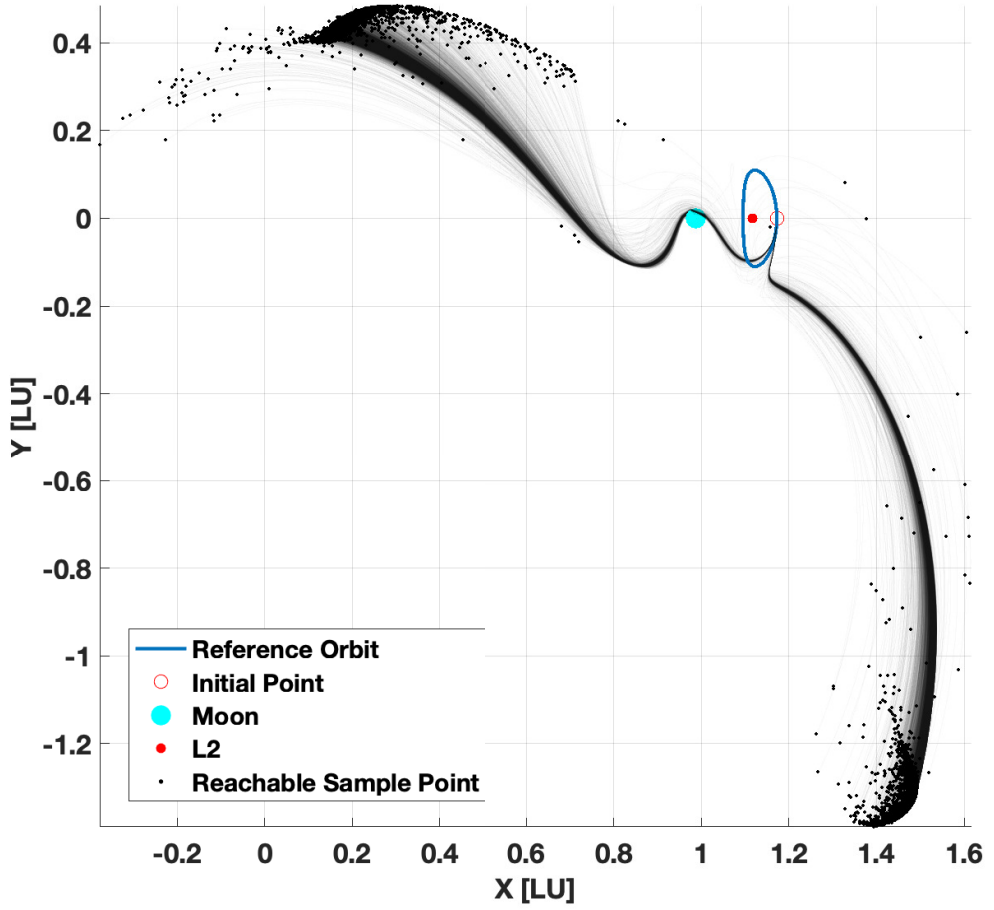

(**b**) XY view of the position reachable set.

Figure 12. Position reachable set over a 350 h time horizon with 10,000 samples.

5.3. Reachability from the Lunar Gateway 9:2 Near Rectilinear Halo Orbit (Case 3)

Case 3 considers the reachable set for the Lunar Gateway earmarked 9:2 NRHO. A low-thrust spacecraft with $T_{\max} = 0.2$ N, $I_{sp} = 3000$ s, and $m_0 = 1000$ kg is used. The period of the L2 reference orbit is 157.500622 h. The initial state vector is given in nondimensionalized

coordinates as $\boldsymbol{x} = [1.0221, 0, -0.1821, 0, -0.1033, 0]^\top$ [61]. All results are computed with a 75 h time horizon and 2000 sample trajectories. The region in the vicinity of the 9:2 NRHO will become a congested area in the near future, so it is imperative to be able to compute reachable sets to perform accurate spacecraft proximity operations in this space and execute potential collision-avoidance maneuvers.

Figure 13 presents the computed reachable set. This result shows a new characteristic of the reachable set: the reachable set not only expands, but also contracts with this time horizon. Before the spacecraft reaches the perilune of the 9:2 NRHO reference orbit, the reachable set expands in a manner consistent with previous results. At perilune, the natural CR3BP dynamics contract the reachable set before expanding again after perilune.

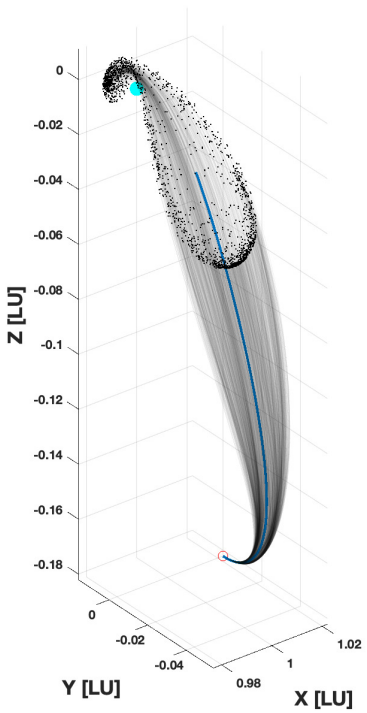

(**a**)

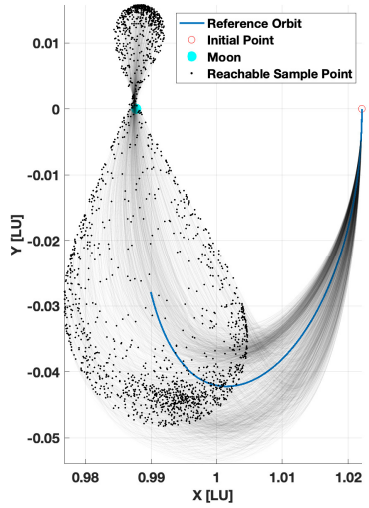

(**b**)

Figure 13. Position reachable set over a 75 h time horizon with 2000 samples. (**a**) Three-dimensional view of the position reachable set. (**b**) XY view of the position reachable set.

5.4. Connection between Reachable Sets and Invariant Manifolds in CR3BP

Historically, low-energy transfers in three-body dynamical models originated with the idea of invariant manifolds. These dynamical structures exist in the vicinity of the circular restricted three-body libation points and can be used to connect trajectories across vast distances in space [69]. An observation from the results presented for a low-thrust spacecraft in the CR3BP dynamics reveals an interesting behavior over long time-horizon values, namely the reachable set exhibits a bifurcation (i.e., there exist "two" different directions leading to reachable sets starting from the same initial condition). Additionally, when all the sampled minimum-time trajectories are plotted, they appear to be clustering around some unknown dynamical structure in the CR3BP dynamics. Examining the structure of the presented algorithm, the terminal costates are sampled from a six-dimensional hypersphere, which implies that the reconstructed thrust vector should be affected by the sampling algorithm. However, some of the thrust vector directions appear to be "more likely" due to the chaotic nature of the CR3BP dynamics. We now attempt to explain this phenomenon of a thrust vector sampling and the distributed reachable set and the clustering of sampled trajectories.

We briefly digress to a discussion of Chaos Theory and the bifurcation of the logistic map. The original 1967 paper by May [70] details how chaos emerges from the iterative solution to the logistic difference equation when the growth rate exceeds 3.570. In the detailed plots of the logistic map, when examining the regions beyond 3.570 with an unstable fixed point, there appear to be some "more" stable points that appear as peaks of a probability distribution in the chaotic region. These are referred to as supertracks [71]. Returning to the analysis of the reachable sets in the CR3BP dynamics, we hypothesize that the clustering of the sampled reachable trajectories is analogous to the supertracks of the logistic map. The CR3BP dynamics is a chaotic one similar to the logistic map in that there exist stable manifolds and libation points. We ascertain that the clustering of sample trajectories is coincident with the invariant manifolds that exist as quasi-stable/unstable structures in the CR3BP dynamics.

To empirically validate our hypothesis, the invariant manifolds associated with the considered L2 Halo orbit are computed. These invariant manifolds are overlaid on the results from the reachable set analysis. The invariant manifolds are computed according to the process outlined in [72,73] and are straightforward to construct using the IMF. The invariant manifolds associated with the reference L2 Halo orbit are shown in Figure 14 for a short time horizon. The motivation for this brief discussion about invariant manifolds is to explain the bifurcation and reachable sample trajectory clustering observed in Figure 12. The unstable and stable manifolds are computed for this same L2 Halo reference periodic orbit and then overlaid onto the reachable set results from Figure 12 to identify any possible trends in the reachable trajectories arising from underlying dynamical structures associated with the chosen periodic orbit.

Figure 15 presents the reachable set with the associated invariant manifolds for the 350 h L2 Halo reference orbit. For this long time horizon, there is a clear direct relationship indicating the tendency for reachable set sample trajectories to cluster on the invariant manifolds. It is important to note that the invariant manifolds propagate in two primary directions originating at the periodic orbit, which is due to the integration in both the forward and backward directions due to stable and unstable manifolds [73]. Since the reachable set, by definition, is the set of all possible states that could be achieved from a given initial condition, it is expected that the sample points terminating the furthest linear distance from the initial condition arrive at the terminal point by exploiting the invariant manifold structure existing in the CR3BP dynamics. Additionally, since the propulsion system used for this model (0.2 N) leads to an overall small perturbation acceleration, the reachable set evolution on this time horizon is expected to be dominated more by the dynamics in the CR3BP dynamics than by the onboard propulsion system. That is, there is a higher probability of a reachable sample point terminating near an invariant manifold than at any other random spatial coordinate, making these invariant manifolds

essentially analogous to supertracks in a general chaotic dynamical system. To the best of our knowledge, the relationship between the reachable set of low-thrust trajectories and invariant manifolds in the CR3BP dynamics has not been identified in the literature.

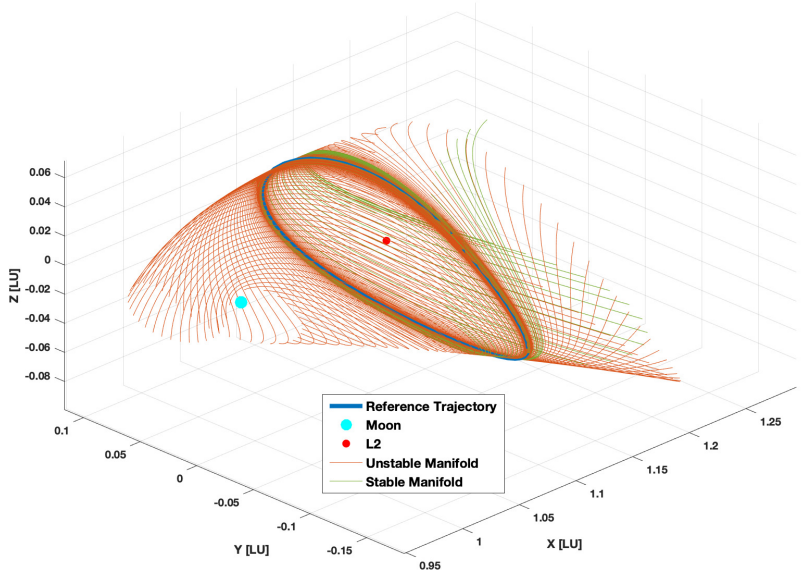

Figure 14. Stable and unstable invariant manifolds of the Earth–Moon L2 Halo orbit.

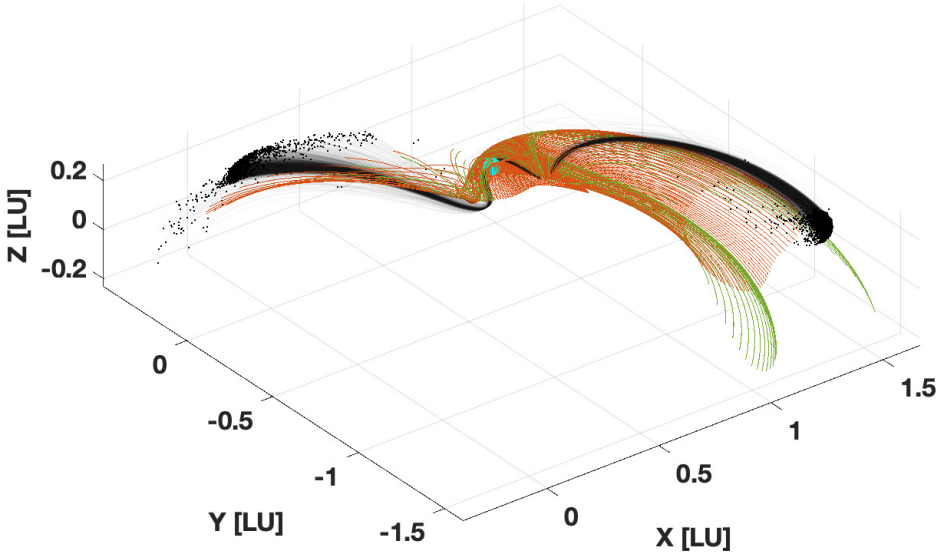

(**a**) Three-dimensional view

Figure 15. *Cont.*

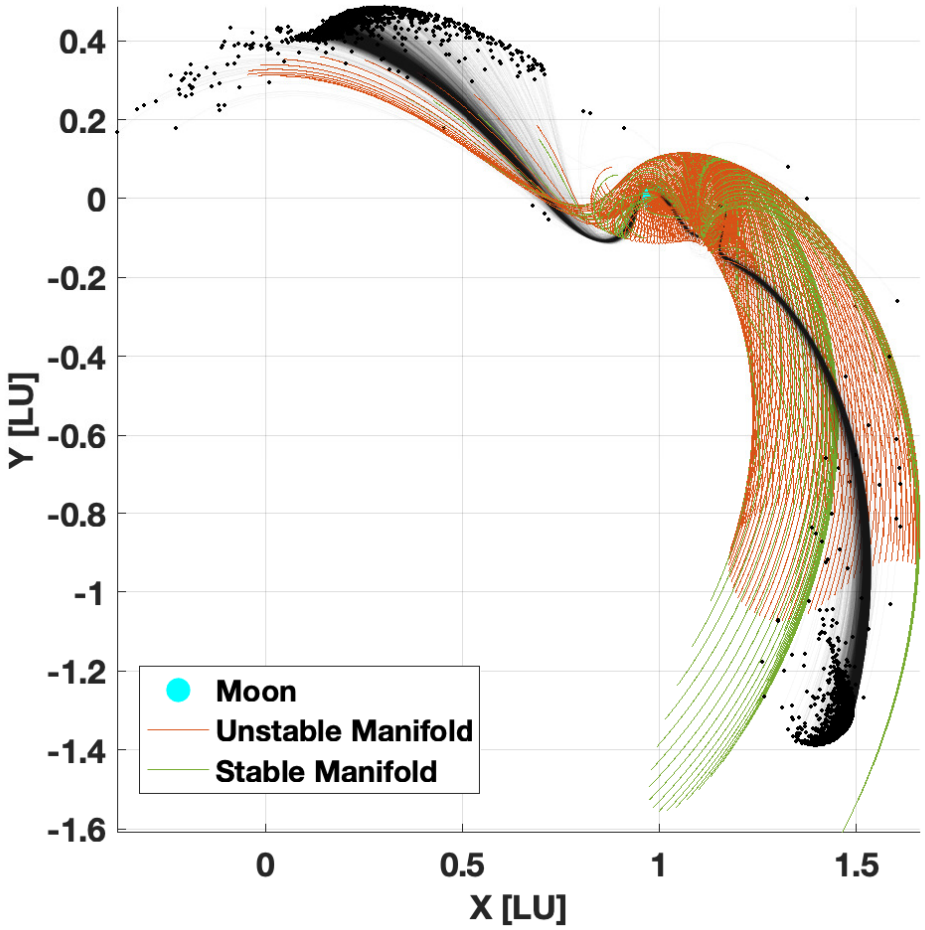

(**b**) XY view

Figure 15. Reachable set overlaid with invariant manifolds for the 350 h L2 reference orbit.

Remarks: Please note that the proposed method is based on rigorous formulations of OCPs (i.e., the variational approach to optimal control). In particular, the class of minimum-time trajectory optimization problems is formulated and studied. The proposed method is sampling-based and is amenable to parallel implementation for rapid approximation of reachable sets. We emphasize that the change in mass of the spacecraft is not neglected but rather integrated analytically. In fact, the dynamics are fully nonlinear. We hope that our method enables researchers and astrodynamicists experts to have an efficient tool for addressing the urgent and interesting problem of approximating the reachable sets of low-thrust spacecraft in complex dynamic regimes, including cislunar space.

6. Conclusions

The indirect multi-stage formulation of optimal control theory was used to implement a rapid reachable set approximation algorithm. A minimum-time low-thrust trajectory formulation was used to recover minimum-time trajectories corresponding to reachable sets. Results are presented detailing the application of this algorithm to a minimum-time Earth-to-Mars transfer. The results indicate that the minimum-time rendezvous lies on the interior of the reachable position set and on the boundary of the reachable velocity set. The effects of injecting initial condition uncertainty and an impulsive maneuver were also evaluated, showing variations in the reachable set.

Novel results detailing the reachable set for low-thrust spacecraft in circular restricted three-body problem (CR3BP) dynamics are presented for L1 point, L2 Halo, and Lunar Gateway 9:2 NRHO reference conditions. Theoretical insight into the behavior of the

reachable set, subject to multi-body perturbations, is provided to show that the reachable set and the invariant manifold structures closely align. The results indicate a new characteristic of the reachable set: the reachable set not only expands but also contracts with the time horizon for the Lunar Gateway 9:2 NRHO case. The presented numerical results for the CR3BP indicate that accurate and rapid determination of reachable sets is possible with a sufficiently large sample of points. In general, reachable sets are typically useful over short time horizons. Thus, sampling-based methods offer a rapid reachable set determination methodology, which is the most likely application for a space-domain awareness situation.

The power of using the proposed sampling method lies in the ability to recover the true reachable set from an HJB solution. The results presented are accurate approximations of the reachable sets of low-thrust spacecraft that can be used to inform grid-based HJB solvers. This means that a mission designer can use the proposed tool to rapidly generate approximate reachable sets, make a decision on whether maneuvers are required (due to collision avoidance, rendezvous, etc.), and feed the approximation to assist a high-fidelity solver that will be used to determine exact reachable boundaries for maneuvering.

Author Contributions: Conceptualization, S.B. and E.T.; Methodology, S.B. and E.T.; Software, S.B. and E.T.; Validation, S.B. and E.T.; Writing—original draft, S.B.; Writing—review & editing, E.T.; Supervision, E.T. All authors have read and agreed to the published version of the manuscript.

Funding: This research received no external funding.

Data Availability Statement: The data presented in this study is available upon request to the authors at ezt0028@auburn.edu.

Acknowledgments: The authors would like to thank Prashant Patel for the fruitful discussions about the indirect multi-stage formulation.

Conflicts of Interest: The authors declare no conflicts of interest. The first author would like to emphasize that the views expressed in this article are those of the authors and do not reflect the official policy or position of the United States Air Force, Department of Defense, or the U.S. Government.

Appendix A. Six-Dimensional Costate Sampling Algorithm

Sampling from a six-dimensional sphere is a step in the proposed method. A general n-dimensional unit sphere can be parameterized in spherical coordinates by $(n-1)$ angles $\phi_1, \ldots, \phi_{n-2} \in [0, \pi]$ and $\phi_{n-1} \in [0, 2\pi]$ [74]. We can randomly sample an $(n-1)$ vector of angles using the MATLAB function `rand`. Algorithm A1 summarizes the steps.

Algorithm A1: Six-dimensional costate sampling algorithm

Result: $\boldsymbol{\lambda}^N$
$n \leftarrow 6$;
$\boldsymbol{\phi} \leftarrow \pi *$ rand$(n-2, 1)$; /* Angles $\phi_1, \ldots, \phi_{n-2} \in [0, \pi]$ */
$\boldsymbol{\phi}(n-1) \leftarrow 2\pi *$ rand ; /* Angle $\phi_{n-1} \in [0, 2\pi]$ */
$\boldsymbol{\lambda}^N(1) \leftarrow \cos(\boldsymbol{\phi}(1))$;
$\boldsymbol{\lambda}^N(2) \leftarrow \sin(\boldsymbol{\phi}(1)) \cos(\boldsymbol{\phi}(2))$;
$\boldsymbol{\lambda}^N(3) \leftarrow \sin(\boldsymbol{\phi}(1)) \sin(\boldsymbol{\phi}(2)) \cos(\boldsymbol{\phi}(3))$;
$\boldsymbol{\lambda}^N(4) \leftarrow \sin(\boldsymbol{\phi}(1)) \sin(\boldsymbol{\phi}(2)) \sin(\boldsymbol{\phi}(3)) \cos(\boldsymbol{\phi}(4))$;
$\boldsymbol{\lambda}^N(5) \leftarrow \sin(\boldsymbol{\phi}(1)) \sin(\boldsymbol{\phi}(2)) \sin(\boldsymbol{\phi}(3)) \sin(\boldsymbol{\phi}(4)) \cos(\boldsymbol{\phi}(5))$;
$\boldsymbol{\lambda}^N(6) \leftarrow \sin(\boldsymbol{\phi}(1)) \sin(\boldsymbol{\phi}(2)) \sin(\boldsymbol{\phi}(3)) \sin(\boldsymbol{\phi}(4)) \sin(\boldsymbol{\phi}(5))$;

References

1. Bertrand, R.; Epenoy, R. New smoothing techniques for solving bang–bang optimal control problems—numerical results and statistical interpretation. *Optim. Control. Appl. Methods* **2002**, *23*, 171–197. [CrossRef]
2. Trélat, E. Optimal control and applications to aerospace: Some results and challenges. *J. Optim. Theory Appl.* **2012**, *154*, 713–758. [CrossRef]

3. Taheri, E.; Li, N. L2 Norm-Based Control Regularization for Solving Optimal Control Problems. *IEEE Access* **2023**, *11*, 125959–125971. [CrossRef]
4. Kovryzhenko, Y.; Taheri, E. Vectorized Trigonometric Regularization for Singular Control Problems with Multiple State Path Constraints. *J. Astronaut. Sci.* **2023**, *71*, 1. [CrossRef]
5. Nurre, N.P.; Taheri, E. Duty-cycle-aware low-thrust trajectory optimization using embedded homotopy. *Acta Astronaut.* **2023**, *212*, 630–642. [CrossRef]
6. Allen, R.E.; Clark, A.A.; Starek, J.A.; Pavone, M. A machine learning approach for real-time reachability analysis. In Proceedings of the 2014 IEEE/RSJ International Conference on Intelligent Robots and Systems, Chicago, IL, USA, 14–18 September 2014; pp. 2202–2208. [CrossRef]
7. Liu, E.; Yan, Y.; Yang, Y. Analysis and determination of capture area for space debris removal based on reachable domain. *Adv. Space Res.* **2021**, *68*, 1613–1626. [CrossRef]
8. Vendl, J.K.; Holzinger, M.J. Cislunar periodic orbit analysis for persistent space object detection capability. *J. Spacecr. Rocket.* **2021**, *58*, 1174–1185. [CrossRef]
9. Chen, Q.; Qiao, D.; Wen, C. Reachable Domain of Spacecraft after a Gravity-Assist Flyby. *J. Guid. Control. Dyn.* **2019**, *42*, 931–940. [CrossRef]
10. Wu, C.Y.; Russell, R.P. Reachable set of low-delta-v trajectories following a gravity-assist flyby. *J. Spacecr. Rocket.* **2023**, *60*, 616–633. [CrossRef]
11. Kirk, D.E. *Optimal Control Theory: An Introduction*; Prentice-Hall Networks Series; Prentice-Hall: Englewood Cliffs, NJ, USA, 1970.
12. Crandall, M.G.; Evans, L.C.; Lions, P.L. Some properties of viscosity solutions of Hamilton-Jacobi equations. *Trans. Am. Math. Soc.* **1984**, *282*, 487–502. [CrossRef]
13. Borrelli, F.; Bemporad, A.; Morari, M. *Predictive Control for Linear and Hybrid Systems*, 1st ed.; Cambridge University Press: Cambridge, UK, 2017. [CrossRef]
14. Wallace, S.W. (Ed.) *Applications of Stochastic Programming*; MPS-SIAM Series on Optimization; Society for Industrial and Applied Mathematics: Philadelphia, PA, USA, 2005.
15. Chen, Q.; Qiao, D.; Wen, C. Minimum-Fuel Low-Thrust Trajectory Optimization via Reachability Analysis and Convex Programming. *J. Guid. Control. Dyn.* **2021**, *44*, 1036–1043. [CrossRef]
16. Vinter, R. A Characterization of the Reachable Set for Nonlinear Control Systems. *SIAM J. Control. Optim.* **1980**, *18*, 599–610. [CrossRef]
17. Jiang, X.; Xia, G.; Feng, Z.; Zheng, W.X.; Su, R. Reachable Set Estimation of Multi-Agent Systems: An Approximate Consensus Perspective. *IEEE Trans. Control. Netw. Syst.* **2023**, *11*, 353–363. [CrossRef]
18. Mitchell, I.; Bayen, A.; Tomlin, C. A time-dependent Hamilton-Jacobi formulation of reachable sets for continuous dynamic games. *IEEE Trans. Autom. Control* **2005**, *50*, 947–957. [CrossRef]
19. Girard, A.; Guernic, C.L. Efficient Reachability Analysis for Linear Systems using Support Functions. *IFAC Proc. Vol.* **2008**, *41*, 8966–8971. [CrossRef]
20. Asarin, E.; Dang, T.; Girard, A. Reachability Analysis of Nonlinear Systems Using Conservative Approximation. In *Hybrid Systems: Computation and Control*; Goos, G., Hartmanis, J., Van Leeuwen, J., Maler, O., Pnueli, A., Eds.; Lecture Notes in Computer Science; Springer: Berlin/Heidelberg, Germany, 2003; Volume 2623, pp. 20–35. [CrossRef]
21. Bansal, S.; Tomlin, C.J. Deepreach: A deep learning approach to high-dimensional reachability. In Proceedings of the 2021 IEEE International Conference on Robotics and Automation (ICRA), Xi'an, China, 30 May–5 June 2021; IEEE: Piscataway, NJ, USA, 2021; pp. 1817–1824. [CrossRef]
22. Xue, D.; Li, J.; Baoyin, H.; Jiang, F. Reachable Domain for Spacecraft with a Single Impulse. *J. Guid. Control. Dyn.* **2010**, *33*, 934–942. [CrossRef]
23. Zhang, G.; Cao, X.; Ma, G. Reachable domain of spacecraft with a single tangent impulse considering trajectory safety. *Acta Astronaut.* **2013**, *91*, 228–236. [CrossRef]
24. Chen, Q.; Qiao, D.; Shang, H.; Liu, X. A new method for solving reachable domain of spacecraft with a single impulse. *Acta Astronaut.* **2018**, *145*, 153–164. [CrossRef]
25. Duan, J.; Liu, Y.; Ding, R. Simple Method to Determine Reachable Domain of Spacecraft with a Single Impulse. *J. Guid. Control. Dyn.* **2019**, *42*, 168–174. [CrossRef]
26. Wen, C.; Zhao, Y.; Shi, P. Precise Determination of Reachable Domain for Spacecraft with Single Impulse. *J. Guid. Control. Dyn.* **2014**, *37*, 1767–1779. [CrossRef]
27. Li, X.; He, X.; Zhong, Q.; Song, M. Reachable domain for satellite with two kinds of thrust. *Acta Astronaut.* **2011**, *68*, 1860–1864. [CrossRef]
28. Vinh, N.X.; Gilbert, E.G.; Howe, R.M.; Sheu, D.; Lu, P. Reachable domain for interception at hyperbolic speeds. *Acta Astronaut.* **1995**, *35*, 1–8. [CrossRef]
29. Wen, C.; Zhao, Y.; Shi, P.; Hao, Z. Orbital Accessibility Problem for Spacecraft with a Single Impulse. *J. Guid. Control. Dyn.* **2014**, *37*, 1260–1271. [CrossRef]
30. Lu, L.; Li, H.; Zhou, W.; Liu, J. Design and analysis of a direct transfer trajectory from a near rectilinear halo orbit to a low lunar orbit. *Adv. Space Res.* **2021**, *67*, 1143–1154. [CrossRef]

31. Wen, C.; Sun, Y.; Peng, C.; Qiao, D. Reachable Domain Under J2 Perturbation for Satellites with a Single Impulse. *J. Guid. Control. Dyn.* **2023**, *46*, 64–79. [CrossRef]
32. Wen, C.; Gao, Y. Reachability Study for Spacecraft Maneuvering from a Distant Retrograde Orbit in the Earth-Moon System. In *AIAC18: 18th Australian International Aerospace Congress (2019): HUMS—11th Defence Science and Technology (DST) International Conference on Health and Usage Monitoring (HUMS 2019): ISSFD—27th International Symposium on Space Flight Dynamics (ISSFD)*; Engineers Australia, Royal Aeronautical Society: Melbourne, Australia, 2019; pp. 1666–1673.
33. Komendera, E.; Scheeres, D.; Bradley, E. Intelligent Computation of Reachability Sets for Space Missions. In Proceedings of the Twenty-Fourth Innovative Applications of Artificial Intelligence Conference, Toronto, ON, Canada, 22–26 July 2012; Volume 26, pp. 2299–2304. [CrossRef]
34. Chernick, M.; D'Amico, S. Closed-Form Optimal Impulsive Control of Spacecraft Formations Using Reachable Set Theory. *J. Guid. Control. Dyn.* **2021**, *44*, 25–44. [CrossRef]
35. Xia, C.; Zhang, G.; Geng, Y. Reachable domain with a single coplanar impulse considering the target-visit constraint. *Adv. Space Res.* **2022**, *69*, 3847–3855. [CrossRef]
36. Lin, X.; Zhang, G. Continuous-Thrust Reachable Set for Linear Relative Motion Near Elliptical Orbits. *IEEE Trans. Aerosp. Electron. Syst.* **2023**, *59*, 9117–9127. [CrossRef]
37. Pang, B.; Wen, C. Reachable Set of Spacecraft With Finite Thrust Based on Grid Method. *IEEE Trans. Aerosp. Electron. Syst.* **2022**, *58*, 2720–2731. [CrossRef]
38. Lee, S.; Hwang, I. Reachable set computation for spacecraft relative motion with energy-limited low-thrust. *Aerosp. Sci. Technol.* **2018**, *77*, 180–188. [CrossRef]
39. Wang, Z.; Jiang, F. Analytical Optimal Solution for the Reachable Domain of Low-Thrust Spacecraft. *J. Spacecr. Rocket.* **2023**, *61*, A35788. [CrossRef]
40. Surovik, D.A.; Scheeres, D.J. Adaptive Reachability Analysis to Achieve Mission Objectives in Strongly Non-Keplerian Systems. *J. Guid. Control. Dyn.* **2015**, *38*, 468–477. [CrossRef]
41. Wen, C.; Qiao, D. Calculating collision probability for long-term satellite encounters through the reachable domain method. *Astrodynamics* **2022**, *6*, 141–159. [CrossRef]
42. Holzinger, M.J.; Scheeres, D.J.; Erwin, R.S. On-Orbit Operational Range Computation Using Gauss's Variational Equations with J2 Perturbations. *J. Guid. Control. Dyn.* **2014**, *37*, 608–622. [CrossRef]
43. Wen, C.; Peng, C.; Gao, Y. Reachable domain for spacecraft with ellipsoidal Delta-V distribution. *Astrodynamics* **2018**, *2*, 265–288. [CrossRef]
44. Holzinger, M.J.; Scheeres, D.J. Reachability Results for Nonlinear Systems with Ellipsoidal Initial Sets. *IEEE Trans. Aerosp. Electron. Syst.* **2012**, *48*, 1583–1600. [CrossRef]
45. Bando, M.; Scheeres, D.J. Nonlinear Attractive and Reachable Sets Under Optimal Control in Three-Body Problem. *J. Guid. Control. Dyn.* **2018**, *41*, 1766–1775. [CrossRef]
46. Kulumani, S.; Lee, T. Systematic Design of Optimal Low-Thrust Transfers for the Three-Body Problem. *J. Astronaut. Sci.* **2019**, *66*, 1–31. [CrossRef]
47. Kousik, S.; Vaskov, S.; Bu, F.; Johnson-Roberson, M.; Vasudevan, R. Bridging the gap between safety and real-time performance in receding-horizon trajectory design for mobile robots. *Int. J. Robot. Res.* **2020**, *39*, 1419–1469. [CrossRef]
48. Kousik, S.; Holmes, P.; Vasudevan, R. Safe, aggressive quadrotor flight via reachability-based trajectory design. In Proceedings of the Dynamic Systems and Control Conference, Park City, UT, USA, 8–11 October 2019; American Society of Mechanical Engineers: New York, NY, USA, 2019; Volume 59162.
49. Bird, T.J.; Pangborn, H.C.; Jain, N.; Koeln, J.P. Hybrid zonotopes: A new set representation for reachability analysis of mixed logical dynamical systems. *Automatica* **2023**, *154*, 111107. [CrossRef]
50. Taheri, E.; Junkins, J.L. How Many Impulses Redux. *J. Astronaut. Sci.* **2020**, *67*, 257–334. [CrossRef]
51. Patel, P.R.; Scheeres, D.J. No Initial Guess Required: Rapidly Computing the Feasible Set of Fuel-Optimal Electric Propulsion Trajectories. In Proceedings of the 33rd AAS/AIAA Space Flight Mechanics Meeting, Austin, TX, USA, 15–19 January 2023; pp. 1–21.
52. Patel, P.R.; Scheeres, D.J. Rapidly and Automatically Estimating Reachability of Electric Propulsion Spacecraft. In Proceedings of the 23rd Advanced Maui Optical and Space Surveillance Technologies Conference, Maui, HI, USA, 27–30 September 2022; pp. 1–15.
53. Bowerfind, S.; Taheri, E. Application of Indirect Multi-Stage Reachable Set Determination Algorithm for Low-Thrust Spacecraft Trajectory Optimization. In Proceedings of the AIAA SCITECH 2024 Forum, Orlando, FL, USA, 8–12 January 2024; p. 0632. [CrossRef]
54. Bryson, A.E.; Ho, Y.C. *Applied Optimal Control: Optimization, Estimation, and Control*, Revised ed.; Cambridge University Press: Cambridge, UK, 1975.
55. Bate, R.R.; Mueller, D.D.; White, J.E. *Fundamentals of Astrodynamics*; Dover Publications: New York, NY, USA, 1971.
56. Taheri, E.; Junkins, J.L. Generic smoothing for optimal bang-off-bang spacecraft maneuvers. *J. Guid. Control. Dyn.* **2018**, *41*, 2470–2475. [CrossRef]
57. Taheri, E.; Li, N.I.; Kolmanovsky, I. Co-state initialization for the minimum-time low-thrust trajectory optimization. *Adv. Space Res.* **2017**, *59*, 2360–2373. [CrossRef]

58. Junkins, J.L.; Taheri, E. Exploration of Alternative State Vector Choices for Low-Thrust Trajectory Optimization. *J. Guid. Control. Dyn.* **2019**, *42*, 47–64. [CrossRef]
59. Patel, P.R.; Scheeres, D.J. Reachable and Fuel-Optimal Trajectory Estimates for Electric Propulsion Spacecraft. In Proceedings of the 2023 IEEE Aerospace Conference, Big Sky, MT, USA, 4–11 March 2023; pp. 1–11.
60. Patel, P.R.; Scheeres, D.J. Rapid and Automatic Reachability Estimation of Electric Propulsion Spacecraft. *J. Astronaut. Sci.* **2023**, *70*, 45. [CrossRef]
61. Thangavelu, C. Transfers between Near Rectilinear Halo Orbits and Low Lunar Orbits. Master's Thesis, University of Colorado, Boulder, CO, USA, 2019.
62. Schaub, H.; Junkins, J.L. *Analytical Mechanics of Space Systems*, 2nd ed.; American Institute of Aeronautics and Astronautics: Reston, VA, USA, 2009. [CrossRef]
63. Conway, B.A. *Spacecraft Trajectory Optimization*; Cambridge University Press: Cambridge, UK, 2010; Volume 29.
64. Bowerfind, S.R.; Taheri, E. Rapid Determination of Low-Thrust Spacecraft Reachable Sets in Two-Body and Cislunar Problems. *arXiv* **2023**, arXiv:2312.08191. [CrossRef]
65. Taheri, E.; Kolmanovsky, I.; Atkins, E. Enhanced Smoothing Technique for Indirect Optimization of Minimum-Fuel Low-Thrust Trajectories. *J. Guid. Control. Dyn.* **2016**, *39*, 2500–2511. [CrossRef]
66. Andersson, J.A.; Gillis, J.; Horn, G.; Rawlings, J.B.; Diehl, M. CasADi: A software framework for nonlinear optimization and optimal control. *Math. Program. Comput.* **2019**, *11*, 1–36. [CrossRef]
67. Jones, R.; Curtis, D.; Zagaris, C. Reachable Set Approximation in Cislunar Space with Pseudospectral Method and Homotopy. In Proceedings of the 2023 IEEE Aerospace Conference, Big Sky, MT, USA, 4–11 March 2023; pp. 1–7. [CrossRef]
68. Trofimov, S.; Shirobokov, M.; Tselousova, A.; Ovchinnikov, M. Transfers from near-rectilinear halo orbits to low-perilune orbits and the Moon's surface. *Acta Astronaut.* **2020**, *167*, 260–271. [CrossRef]
69. Mingotti, G.; Sánchez, J.; McInnes, C. Combined low-thrust propulsion and invariant manifold trajectories to capture NEOs in the Sun–Earth circular restricted three-body problem. *Celest. Mech. Dyn. Astron.* **2014**, *120*, 309–336. [CrossRef]
70. May, R.M. Simple mathematical models with very complicated dynamics. *Nature* **1976**, *261*, 459–467. [CrossRef] [PubMed]
71. Oblow, E. Supertracks, supertrack functions and chaos in the quadratic map. *Phys. Lett. A* **1988**, *128*, 406–412. [CrossRef]
72. Koon, W.; Lo, M.; Marsden, J.; Ross, S. Dynamical Systems, the Three-Body Problem and Space Mission Design. In *Interdisciplinary Applied Mathematics*; Springer: Berlin/Heidelberg, Germany, 2011.
73. Singh, S.; Junkins, J.; Anderson, B.; Taheri, E. Eclipse-Conscious Transfer to Lunar Gateway Using Ephemeris-Driven Terminal Coast Arcs. *J. Guid. Control. Dyn.* **2021**, *44*, 1972–1988. [CrossRef]
74. Blumenson, L. A derivation of n-dimensional spherical coordinates. *Am. Math. Mon.* **1960**, *67*, 63–66. [CrossRef]